



Published in final edited form as:

Neuron. 2017 August 02; 95(3): 591–607.e10. doi:10.1016/j.neuron.2017.07.004.

Molecular mechanisms of synaptic vesicle priming by Munc13 and Munc18

Ying Lai^{1,2,3,4,5,¶}, Ucheor B. Choi^{1,2,3,4,5,¶}, Jeremy Leitz^{1,2,3,4,5}, Hong Jun Rhee⁶, Choongku Lee⁶, Bekir Altas⁶, Minglei Zhao^{1,2,3,4,5}, Richard A. Pfuetzner^{1,2,3,4,5}, Austin L. Wang^{1,2,3,4,5}, Nils Brose⁶, JeongSeop Rhee⁶, and Axel T. Brunger^{1,2,3,4,5,7,*}

¹Department of Molecular and Cellular Physiology, Stanford University, Stanford, United States

²Department of Neurology and Neurological Science, Stanford University, Stanford, United States

³Department of Structural Biology, Stanford University, Stanford, United States

⁴Department of Photon Science, Stanford University, Stanford, United States

⁵Howard Hughes Medical Institute, Stanford University, Stanford, United States

⁶Department of Molecular Neurobiology, Max Planck Institute for Experimental Medicine, Göttingen, Germany

SUMMARY

Munc13 catalyzes the transit of syntaxin from a closed complex with Munc18 into the ternary SNARE complex. Here we report a new function of Munc13, independent of Munc18: it promotes the proper syntaxin / synaptobrevin subconfiguration during assembly of the ternary SNARE complex. In cooperation with Munc18, Munc13 additionally ensures the proper syntaxin / SNAP-25 subconfiguration. In a reconstituted fusion assay with SNAREs, complexin, and synaptotagmin, inclusion of both Munc13 and Munc18 quadruples the Ca²⁺-triggered amplitude and achieves Ca²⁺-sensitivity near physiological concentrations. In Munc13-1/2 double-knockout neurons, expression of a constitutively open mutant of syntaxin could only minimally restore neurotransmitter release relative to Munc13-1 rescue. Together, the physiological functions of Munc13 may be related to regulation of proper SNARE complex assembly.

Keywords

neurotransmitter release; neuronal SNAREs; synaptotagmin; complexin; Munc13; Munc18; priming; plasticity

*For correspondence: brunger@stanford.edu.

¶Lead contact

¶These authors contributed equally to this work.

Author Contributions

Y.L. performed the fusion experiments, U.B.C. the single molecule fluorescence experiments, and H.J.R., B.A., C.K.L and J.R. the neuronal culture experiments. R.A.P., A. L.W., U.B.C. and M.Z. expressed and purified proteins. Y.L., U.B.C., N.B., and J.R. analyzed the data. Y.L., U.B.C., J.R., and A.T.B. designed the experiments. Y.L., U.B.C., R.A.P., A.L.W., J.L., J.R., and A.T.B. wrote the manuscript.

INTRODUCTION

Membrane fusion of synaptic vesicles is an essential process for neurotransmitter release in the nervous system (Südhof, 2013; Rothman, 2014). The synaptic fusion machinery includes the neuronal SNARE (soluble NSF-attachment protein receptor) proteins synaptobrevin-2 / VAMP2 (Vesicle Associated Membrane Protein 2), syntaxin-1, and SNAP-25 (Synaptosomal-Associated Protein 25); together, they form a *trans* ternary (syntaxin-1 / SNAP-25 / synaptobrevin-2) SNARE complex, bringing the synaptic vesicle and plasma membranes into close juxtaposition and ultimately providing the energy for membrane fusion (Sutton et al., 1998; Weber et al., 1998). The Ca²⁺-sensor synaptotagmin is essential for evoked neurotransmission (Geppert et al., 1994; Fernández-Chacón et al., 2001). The main isoform involved in fast synchronous release, synaptotagmin-1, forms a conserved, Ca²⁺-independent “primary” interface with the neuronal ternary SNARE complex (Zhou et al., 2015). Complexin-1, a small cytosolic α -helix protein abundant in the presynaptic terminal (McMahon et al., 1995), cooperates with synaptotagmin-1 to activate Ca²⁺-triggered neurotransmitter release and it also regulates spontaneous neurotransmitter release (Mohrmann et al., 2015; Trimbuch and Rosenmund, 2016). In addition to the primary interface, another synaptotagmin-1 molecule forms a tripartite interface with both the SNARE complex and complexin-1 (Zhou et al., 2017).

Prior to Ca²⁺-triggered neurotransmitter release, synaptic vesicles are “primed”, a process that enables the synaptic vesicles to undergo fast-triggered fusion, *i.e.*, to be “readily releasable” upon the arrival of an action potential. Munc13-1 and its homologues are primarily brain-specific, cytoplasmic proteins in the presynaptic terminal that are involved in synaptic vesicle priming and short-term synaptic plasticity (Südhof, 2012, 2013). Neurons in mice lacking Munc13-1 exhibit severely limited activity-dependent neurotransmitter release as well as hypertonic sucrose stimulation that causes fusion of all readily releasable synaptic vesicles (Augustin et al., 1999). Mutation of *unc-13* in *C. elegans* (Richmond et al., 1999) and elimination of *Dunc-13* in *Drosophila* (Aravamudan et al., 1999) also abolishes neurotransmitter release. Munc13-1 and -2 double-knockout mice have essentially no release-competent synaptic vesicles (Varoqueaux et al., 2002) and exhibit a severe docking defect (Imig et al., 2014).

In addition to Munc13, Sec1 / Munc18 (SM) proteins are also required components of all membrane trafficking pathways as exemplified by the block of synaptic vesicle fusion upon Munc18-1 knockout in mice (Verhage et al., 2000). Upon disassembly of SNARE complexes with N-ethylmaleimide-sensitive factor (NSF) and α SNAP (soluble NSF adaptor protein), Munc18-1 captures syntaxin-1A, locking it into a “closed” conformation and preventing reassembly of the ternary SNARE complex (Ma et al., 2013). Munc18-1 binds tightly ($K_d \sim 1\text{--}4$ nM) to syntaxin-1A in which its Habc domain interacts in a *cis* conformation with its SNARE domain (Misura et al., 2000; Chen et al., 2008), in turn hindering reassembly of SNARE complexes (Pevsner et al., 1994; Yang et al., 2000).

Munc13-1 contains a C1 domain, three C2 domains (C2A, C2B, C2C), and a MUN domain. The MUN domain of Munc13-1 (amino acid range 859–1531) catalyzes the transit of syntaxin-1A from the syntaxin-1A / Munc18-1 complex into the ternary SNARE complex

(Basu et al., 2005; Ma et al., 2013; Yang et al., 2015). Earlier studies in *C. elegans* suggested a similar function of full-length *unc-13* (Richmond et al., 2001), although the role of the MUN domain has not been directly studied in that system. The so-called LE mutant of syntaxin-1A (syntaxin-1A^{LE}) (Dulubova et al., 1999) bypasses the requirement of Munc13-1 for the transit of syntaxin-1A into the ternary SNARE complex in presence of SNAP-25A and synaptobrevin-2 *in vitro* (Ma et al., 2011). It accomplishes this by preferentially adopting an open conformation of syntaxin-1A (Fig. 4G in ref. (Wang et al., 2017)). However, this open syntaxin-1A mutant can only partially restore neurotransmitter release in *unc-13* mutants of *C. elegans* (Hammarlund et al., 2007).

Here we report a new additional molecular function of Munc13-1: the MUN domain of Munc13-1 promotes the proper syntaxin-1A / synaptobrevin-2 arrangement within the ternary SNARE complex when it is assembled from the syntaxin-1A / SNAP-25A complex via addition of synaptobrevin-2 *in vitro*. Moreover, when starting from the syntaxin-1A / Munc18-1 complex, Munc13-1 additionally ensures formation of the proper syntaxin-1A / SNAP-25A arrangement in the presence of SNAP-25A and synaptobrevin-2, *i.e.*, Munc13-1 and Munc18-1 act together to ensure the proper assembly of the entire ternary SNARE complex. Inclusion of the MUN domain or the larger C1C2BMUN or C1C2BMUNC2C fragments of Munc13-1 in a fusion assay approximately quadrupled the Ca²⁺-triggered fusion response. When Munc18-1 was included as well, the sensitivity of the assay for Ca²⁺-triggered fusion reached the physiological range.

RESULTS

Munc13-1 promotes the proper syntaxin-1A / synaptobrevin-2 subconfiguration

The properly assembled SNARE complex consists of a parallel four helix bundle (Sutton et al., 1998). However, interacting SNARE domains can assume alternative configurations when the components are mixed in the absence of other factors that assist proper complex formation (Brunger, 2006). In particular, improperly assembled ternary SNARE complexes, including antiparallel configurations, have been observed (Weninger et al., 2003; Choi et al., 2016). These alternative “subconfigurations” are probably kinetically trapped dead-end states. The question arises how the neuronal *trans* ternary SNARE complex is properly assembled *in vivo*.

The syntaxin-1A / SNAP-25A complex is a starting point for the assembly of *trans* ternary SNARE complex (Fasshauer and Margittai, 2004; Weninger et al., 2008), although other complexes have also been implicated as possible starting points or intermediates (Woodbury, 2000; Chen et al., 2001; Ma et al., 2013). We used single molecule fluorescence resonance energy transfer (smFRET) experiments to monitor the assembly of the ternary SNARE complex starting from surface-tethered syntaxin-1A / SNAP-25A complex (Figures 1A–B). Based on the crystal structure of the neuronal SNARE complex (PDB ID 1SFC) (Sutton et al., 1998) we chose labeling sites for syntaxin-1A and synaptobrevin-2 such that the fluorescent label pair should produce high FRET efficiency upon proper assembly of the ternary SNARE complex. The cytoplasmic domain of synaptobrevin-2 was then added to form ternary SNARE complex in the absence (Figure 1A) or presence (Figure 1B) of the

MUN domain at the specified concentration, or alternatively with Bovine Serum Albumen (BSA) as a control.

Labeled synaptobrevin-2 was readily incorporated into ternary SNARE complex starting from the syntaxin-1A / SNAP-25A complex regardless of the presence of the MUN domain or BSA control (Figure 1C and Table S1). Next we examined the FRET efficiency of the label pairs to probe the syntaxin-1A / synaptobrevin-2 subconfiguration within the ternary SNARE complex (Figures 1D–F and Table S2). In the absence of the MUN domain, two distinct FRET efficiency states emerged: a high FRET efficiency state that corresponds to the ternary SNARE complex with the proper parallel syntaxin-1A / synaptobrevin-2 subconfiguration, and a low FRET efficiency state that corresponds to other syntaxin-1A / synaptobrevin-2 subconfigurations, including antiparallel arrangements (Figures 1A and 1D) (Weninger et al., 2003). The stoichiometry of both properly and improperly assembled SNARE complexes is likely 1:1:1 (STAR methods).

When the MUN domain was present during assembly of the ternary SNARE complex, the population of the low FRET efficiency state was reduced as a function of MUN domain concentration, with most of it being suppressed in the presence of 10 μ M MUN domain (Figures 1E–F). In contrast, the BSA control did not suppress the low FRET efficiency population. Thus, the MUN domain promotes the proper syntaxin-1A / synaptobrevin-2 subconfiguration when the ternary SNARE complex is assembled by addition of synaptobrevin-2 to the syntaxin-1A / SNAP-25A complex in the presence of the MUN domain.

We next asked if the MUN domain could likewise promote the proper syntaxin-1A / SNAP-25A subconfiguration within the ternary SNARE complex when assembly is performed by addition of both SNAP-25A and synaptobrevin-2 to syntaxin-1A. Based on the crystal structure of the neuronal SNARE complex (PDB ID 1SFC) (Sutton et al., 1998) we again designed fluorescent labeling sites on syntaxin-1A and SNAP-25A such that the label pair should produce high FRET efficiency when the ternary SNARE complex is properly assembled (Figure 1G). Labeled SNAP-25A was readily incorporated into ternary SNARE complex (Figure 1H and Table S1), regardless of the presence of the MUN domain or BSA control. Using this system, we probed the syntaxin-1A / SNAP-25A subconfiguration within the ternary SNARE complex (Figures 1I–K, Table S2). The smFRET efficiency histogram showed two states regardless of the presence of the MUN domain or BSA control: a high FRET efficiency state that corresponds to the proper assembly of ternary SNARE complex with the proper parallel syntaxin-1A / SNAP-25A subconfiguration in the ternary SNARE complex, and a low FRET efficiency state that corresponds to other syntaxin-1A / SNAP-25A subconfigurations, such as antiparallel arrangements (right panel in Figure 1G) (Weninger et al., 2003) or situations where one of the SNAP-25A α -helices is not fully incorporated into the ternary SNARE complex (Weninger et al., 2008). Thus, while the MUN domain alone promotes the proper syntaxin-1A / synaptobrevin-2 subconfiguration within the ternary SNARE complex, it has no effect on the proper syntaxin-1A / SNAP-25A subconfiguration.

The experiments presented in Figure 1 were performed without the involvement of Munc18-1, suggesting that the MUN domain has an autonomous function independent of Munc18-1. How does the MUN domain induce the proper syntaxin-1A / synaptobrevin-2 subconfiguration during assembly of the ternary SNARE complex? Previous reports showed that the MUN domain interacts with syntaxin-1A as well as with syntaxin-1A / SNAP-25A and ternary SNARE complexes (Guan et al., 2008; Weninger et al., 2008; Ma et al., 2011). However, these experiments did not address the possibility of interactions between the MUN domain and synaptobrevin-2. To re-investigate this question we performed single molecule binding experiments (Figures S1A–C) wherein the cytoplasmic domain of synaptobrevin-2 was labeled with the fluorescent dye Alexa 647 and tethered to a passivated surface. The MUN domain was labeled with the fluorescent dye Alexa 555 and added to the surface-tethered and labeled synaptobrevin-2 molecules. Alternating laser illumination was used to co-localize synaptobrevin-2 and MUN domain molecules. We observed transient binding events, as indicated by the stepwise increases in fluorescence intensity of the fluorescent label attached to the MUN domain (Figure S1A). We generated histograms of the bound and the unbound dwell times, and estimated the on and the off rates by fitting exponential functions to the histograms, respectively (Figures S1B–C). However, due to the low frequency of binding events over the observation period of 200 seconds and the high background of unbound MUN domain molecules at concentrations above 100 nM, the on rate and the resulting dissociation constant obtained by this method may be unreliable.

To further corroborate the binding of synaptobrevin-2 and the MUN domain, we performed bulk fluorescence anisotropy measurements to obtain an estimate of the dissociation constant (K_d). For this experiment, the cytoplasmic domain of synaptobrevin-2 was labeled with the fluorescent dye Alexa 488, and titrated with unlabeled MUN domain at different concentrations. The fluorescence anisotropy curves were fit to a Hill function, resulting in $K_d \sim 109.9 \pm 35.4 \mu\text{M}$ (red line in Figure S1D). To confirm the specificity of this interaction, we performed a competition experiment in the presence of 50 μM of unlabeled cytoplasmic domain of synaptobrevin-2, resulting in a substantial decrease of the binding with labeled synaptobrevin-2 molecules (black line in Figure S1D). For comparison with previously published binding experiments, we measured the interaction between syntaxin-1A and the MUN domain using the cytoplasmic domain of syntaxin-1A that was labeled with the fluorescent dye Alexa 488 (Figure S1E), resulting in $K_d \sim 70.8 \pm 5.9 \mu\text{M}$, close to the previously published dissociation constant $K_d \sim 46 \mu\text{M}$ (Ma et al., 2011).

The MUN domain nearly quadruples Ca^{2+} -triggered vesicle fusion

Since the MUN domain promotes formation of the proper syntaxin-1A / synaptobrevin-2 subconfiguration within the ternary SNARE complex, we asked if this property of the MUN domain has functional consequences in Ca^{2+} -triggered vesicle fusion. We investigated the effect of the MUN domain on Ca^{2+} -independent and Ca^{2+} -triggered fusion using a single vesicle content mixing assay with reconstituted full-length neuronal SNAREs, synaptotagmin-1, and complexin-1 (Lai et al., 2014). Two types of vesicles were reconstituted: vesicles with reconstituted syntaxin-1A and SNAP-25A (referred to as *PM vesicles*) and vesicles with reconstituted synaptobrevin-2 and synaptotagmin-1 that mimic synaptic vesicles (referred to as *SV vesicles*) (Figures 2A and STAR methods).

The PM vesicles were tethered on a passivated surface after preincubation with the MUN domain (protocol “All” in Figure 2A and STAR methods). After washing unbound PM vesicles, SV vesicles were added and incubated for a 1 min period, and then unbound SV vesicles were removed. Subsequently, Ca^{2+} -independent fusion was monitored for 1 min, followed by injection of 500 μM Ca^{2+} , after which Ca^{2+} -triggered fusion was monitored for an additional 1 min period. Complexin-1 was present when SV vesicles were added and in all subsequent stages.

Inclusion of 10 μM MUN domain in the fusion assay had no effect on the intrinsic Ca^{2+} -independent fusion probability (Figures 2B and S2A). We note that Ca^{2+} -independent fusion probabilities obtained from our *in vitro* fusion experiments are normalized with respect to the number of associated vesicles. In contrast, the frequency of spontaneous (mini) release that is measured in electrophysiological experiments depends on both the number of functional synapses as well as the number of synaptic vesicles that are capable of undergoing spontaneous fusion. Moreover, spontaneous fusion in neurons likely depends on another Ca^{2+} sensor that is presently not included in our fusion assay (Xu et al., 2009; Zhou et al., 2017). Therefore, our observed Ca^{2+} -independent vesicle fusion does not necessarily correlate to spontaneous mini release *in vivo*.

The presence of the MUN domain increased the probability of fast Ca^{2+} -triggered fusion (*i.e.*, the Ca^{2+} -triggered amplitude) by a factor of 3.6 (Figures 2C, S2F, and Table S3). We also observed an increase in the ratio of the Ca^{2+} -triggered amplitude to the average probability of Ca^{2+} -independent fusion per second (referred to as “fusion ratio”) by a factor of 3.3 (Figure 2D), and increased the synchronization (decay constant) by a factor of 1.7 (Figure 2E). These increases were dependent on the concentration of the MUN domain.

We next asked the question if the presence of the MUN domain upon Ca^{2+} -triggering (Figure 2A) plays a direct role in Ca^{2+} -triggered fusion. Considering the weak affinity of the MUN domain to SNARE complexes (Guan et al., 2008; Weninger et al., 2008; Ma et al., 2011), we hypothesized that extensive washing could remove any bound MUN domain. Therefore, we repeated the fusion experiment, but extensively washed the SV-PM vesicles with buffer that only contained complexin-1, but not the MUN domain, after vesicle association (protocol “Pre”, Figure 2A). We confirmed that this washing protocol removed all the MUN domain molecules that were present during vesicle association (Figure S3). The extensive washing protocol still increased the Ca^{2+} -triggered amplitude and the fusion ratio compared to levels similar to when the MUN domain is present at all stages of the assay (Figures 2B–D). Conversely, when the MUN domain was added only after vesicle association (protocol “Post”, Figure 2A), the Ca^{2+} -independent fusion rate, Ca^{2+} -triggered amplitude, the fusion ratio, and the Ca^{2+} -triggered synchronization were not changed from levels where the MUN domain was never present (Figures 2B–E). Together these data suggest that the effect of the MUN domain on Ca^{2+} -triggered fusion is a consequence of promoting the proper syntaxin-1A / synaptobrevin-2 subconfiguration, rather than a direct effect on Ca^{2+} -triggered fusion itself.

The C1C2BMUN and C1C2BMUNC2C fragments act similarly to the MUN domain, but at lower concentrations

We next investigated the effect of the larger C1C2BMUN and C1C2BMUNC2C fragments (Liu et al., 2016; Xu et al., 2017) in our fusion assay. We used the same protocol as in Figure 2A except that the MUN domain was replaced with one of these fragments at the specified concentrations (Figures 3A, S2B, S2G, S4 and Table S4). Similar to the MUN domain, inclusion of these fragments in the fusion assay had no effect on the intrinsic Ca^{2+} -independent fusion probability (Figure 3B), but increased the Ca^{2+} -triggered fusion amplitude by a factor of ~ 5 , the fusion ratio by a factor of ~ 4 , and the synchronization by a factor of ~ 1.6 (Figures 3C–E). Moreover, inclusion of the C1C2BMUN and C1C2BMUNC2C fragments achieved similar effects to the MUN domain at a twenty and a hundred fold lower concentration, respectively. As shown in Figure S5, inclusion of the C2C domain in the Munc13 fragment (*i.e.*, C1C2BMUNC2C) increases vesicle association *in vitro*, consistent with an increase of the readily releasable pool upon inclusion of the C2C domain as in neurons (Liu et al., 2016) and chromaffin cells (Stevens et al., 2005). However, due to a relatively low yield of purified C1C2BMUNC2C fragment, we used the C1C2BMUN fragment in all of the following experiments.

The C1 and C2B domains of Munc13-1 bind to DAG and PIP2, respectively (Rhee et al., 2002; Shin et al., 2010), both of which were included in the PM vesicles in the experiments shown above. Even at zero Ca^{2+} concentration there is a weak but significant interaction between C2B and PIP2. When either DAG or both DAG and PIP2 were omitted from the PM vesicles, smaller effects of the C1C2BMUN fragment on Ca^{2+} -triggered fusion were observed (Figures S6C–E and Table S4), suggesting that the DAG - C1 and PIP2 - C2B interactions cooperate in enhancing the effect of the C1C2BMUN fragment on Ca^{2+} -triggered fusion. However, even in the absence of both PIP2 and DAG, inclusion of 0.5 μM C1C2BMUN fragment in the fusion assay slightly increased the Ca^{2+} -triggered fusion amplitude and synchronization (Figures S6C–E).

In the absence of complexin-1, inclusion of the C1C2BMUN fragment in the fusion assay increased both the Ca^{2+} -independent fusion probability and the Ca^{2+} -triggered fusion amplitude (Figure S7 and Table S4). When complexin-1 is included as well, the Ca^{2+} -independent fusion probability is decreased while the Ca^{2+} -triggered fusion amplitude is greatly increased. Likewise, complexin-1 has similar effects on these fusion probabilities in the absence of C1C2BMUN. These experiments show that these two functions of complexin-1 are independent from the inclusion of Munc13-1 or the combination of Munc18-1 and Munc13-1 in the fusion assay.

In neurons, the Ca^{2+} -sensitivity of synaptic vesicle fusion starts at $\sim 10 \mu\text{M}$ and saturates at $\sim 100 \mu\text{M}$ (Heidelberger et al., 1994; Schneggenburger and Neher, 2000). Yet, the best Ca^{2+} -sensitivity that we have been able to achieve in the past with our fusion assay was around 500 μM (Diao et al., 2012). We re-assessed the Ca^{2+} -sensitivity of our fusion assay, but now in the presence of the C1C2BMUN fragment (Figure 3F). We observed a substantial increase in Ca^{2+} -triggered fusion amplitude below 100 μM Ca^{2+} . Fitting the Ca^{2+} -triggered fusion amplitude and the fusion ratio to Hill functions (Figures 3F–G) produced half-maximal Ca^{2+} concentrations of $82 \pm 28 \mu\text{M}$ for the Ca^{2+} -triggered fusion amplitude and 66

$\pm 36 \mu\text{M}$ for the fusion ratio. Although this is already a major improvement of our assay, we describe below how we achieved an even more substantial increase in Ca^{2+} -sensitivity in our fusion assay.

Munc13-1 and Munc18-1 cooperate to properly assemble the ternary SNARE complex

Instead of the syntaxin-1A / SNAP25A complex, the syntaxin-1A / Munc18-1 complex may serve as another starting point for ternary SNARE complex formation upon addition of synaptobrevin-2, SNAP-25, and Munc13-1 (Ma et al., 2013). We asked if the syntaxin-1A / Munc18-1 complex is also a good starting point for proper assembly of ternary SNARE complex. We again used single molecule fluorescence microscopy in order to monitor the assembly of the ternary SNARE complex starting from the syntaxin-1A / Munc18-1 complex (Figures 4A, 4E). We subsequently assembled ternary SNARE complex by addition of SNAP-25A and synaptobrevin-2 in the presence or absence of the MUN domain.

We first assessed the incorporation of labeled synaptobrevin-2 (Figure 4B and Table S1) or labeled SNAP-25A (Figure 4F and Table S1) into ternary SNARE complex starting from the surface-tethered syntaxin-1A / Munc18-1 complex. As expected, the MUN domain was required for the transit of syntaxin-1A into the ternary SNARE complex (Ma et al., 2011; Yang et al., 2015). When the MUN domain concentration was increased, more ternary SNARE complex was formed and, in contrast, BSA control did not lead to ternary complex formation (Figures 4B, 4F and Table S1).

Using FRET label pairs we probed the syntaxin-1A / synaptobrevin-2 subconfiguration (Figures 4C–D and Table S2) and the syntaxin-1A / SNAP-25A subconfiguration (Figures 4G–H and Table S2) within ternary SNARE complexes that were assembled starting from syntaxin-1A / Munc18-1 with the addition of synaptobrevin-2, SNAP-25A, and MUN domain. The smFRET histograms revealed a majority of high FRET efficiency populations ($\sim 95\%$) for both subconfigurations, demonstrating that the MUN domain and Munc18-1 cooperate to properly assemble ternary SNARE complex by promoting both the proper syntaxin-1A / synaptobrevin-2 and syntaxin-1A / SNAP-25A subconfigurations within the ternary SNARE complex.

Inclusion of both Munc18-1 and Munc13-1 leads to near physiological Ca^{2+} -sensitivity in the fusion assay

Since Munc18-1 and Munc13-1 cooperate to promote proper assembly of the ternary SNARE complex (Figure 4), we also wanted to perform our fusion assay starting from reconstituted syntaxin-1A / Munc18-1 complex. However, direct reconstitution of the syntaxin-1A / Munc18-1 complex into liposomes is technically challenging due to poor solubility of the syntaxin-1A / Munc18-1 complex and dissociation of the complex by certain detergents (Rickman and Davletov, 2005). We therefore reconstituted syntaxin-1A / SNAP-25A complex in PM vesicles, followed by addition of the “disassembly factors” (NSF, αSNAP , ATP, Mg^{2+}) along with Munc18-1 similar to previous bulk fusion experiments (Ma et al., 2013).

We first determined the efficiency of formation of the syntaxin-1A / Munc18-1 complex starting from syntaxin-1A / SNAP-25A complex by adding the disassembly factors in the

presence of Munc18-1 using smFRET efficiency experiments (Figure 5 and Tables S5–S6). The surface-tethered cytoplasmic domain of syntaxin-1A was labeled with a pair of dyes, such that high FRET efficiency is expected in the closed state of syntaxin-1A based on the crystal structure of the syntaxin-1A / Munc18-1 complex (Misura et al., 2000) (Figures 5A, 5C, and 5D). Indeed, the syntaxin-1A / Munc18-1 complex exhibits high FRET efficiency corresponding to the closed conformation of syntaxin-1A (Figure 5C bottom panel, Figure 5D red arrow, and Figure 5G) whereas the syntaxin-1A / SNAP-25A SNARE complex shows predominantly low FRET efficiency, corresponding to the open conformation of syntaxin-1A (middle panel in Figure 5C, green line in Figure 5D, and Figure 5G).

Upon disassembly of the syntaxin-1A / SNAP-25A complex with the disassembly factors (Figure 5B), syntaxin-1A sampled a wide range of conformations similar to isolated syntaxin-1A (black line in Figure 5D vs. the blue line in Figure 5E). When Munc18-1 was present in addition to the disassembly factors, syntaxin-1A is primarily in the closed conformation (Figure 5E red line, and Figure 5G). In contrast, formation of the syntaxin-1A / Munc18-1 complex did not occur in the absence of Mg^{2+} since lack of Mg^{2+} prevents ATP hydrolysis (Figures 5F–G). Taken together, the disassembly factors dissociate syntaxin-1A from the syntaxin-1A / SNAP-25A complex, allowing Munc18-1 to capture it.

We applied this disassembly method for formation of the syntaxin-1A / Munc18-1 complex as the starting point for our fusion assay (Figure 6A) (we refer to this experiment as “complete reconstitution”). Robust Ca^{2+} -triggered fusion histograms were observed in the range of 20–500 μM Ca^{2+} (Figures 6B, S2J and Table S7). When comparing the complete reconstituted fusion assay with the assay starting from PM vesicles, without the intervening steps involving Munc18-1 and the disassembly factors, the Ca^{2+} -independent fusion probability is similar (Figure 3B vs. presence of C1C2BMUN in Figure 6C), the 500 μM Ca^{2+} -triggered fusion amplitude and fusion ratio are similar, and the synchronization is slightly improved (0.5 μM C1C2BMUN in Figure 3 vs. presence of C1C2BMUN in Figure 6). In the absence of the C1C2BMUN fragment no fusion events were observed within experimental error (Figures 6C–F), since ternary SNARE complex formation cannot occur starting from the syntaxin-1A / Munc18-1 complex without Munc13-1.

A Ca^{2+} -titration revealed that the complete reconstituted fusion assay (starting from the syntaxin-1A / Munc18-1 complex) was three-fold more sensitive than the fusion assay starting from the syntaxin-1A / SNAP-25A complex (Figure 3F vs. Figure 6G), with half-maximal Ca^{2+} concentrations of $23.1 \pm 2.2 \mu M$ for the Ca^{2+} -triggered fusion amplitude and $23.3 \pm 2.4 \mu M$ for the fusion ratio. In summary, the full reconstitution that includes neuronal SNAREs, synaptotagmin-1, complexin-1, Munc13-1, Munc18-1, NSF, and α SNAP improved the Ca^{2+} -sensitivity in the fusion assay by an order of magnitude, and the Ca^{2+} -sensitivity is now in the physiological range. Taken together, we have reached a major milestone in reconstituting synaptic vesicle fusion.

We note that *in vitro* Ca^{2+} -sensitivity experiments do not necessarily mimic experiments with varying extracellular Ca^{2+} concentration in neurons. Nevertheless, we note that neurons from ELKS and RIM deficient mice exhibit a loss of Munc13 and a lower sensitivity to extracellular Ca^{2+} concentration (Wang et al., 2016). Moreover, manipulations of the Ca^{2+} -

binding regions of the C2A and C2B domains of the distant Munc13-4 homologue resulted in lower Ca^{2+} -sensitivity of granule exocytosis in mast, neuroendocrine, and platelets cells (Boswell et al., 2012).

Overexpression of the syntaxin-1A^{LE} mutant in Munc13-1/2 deficient neurons

As previously reported, the syntaxin-1A^{LE} mutant bypasses the need for Munc13 in promoting the transit into the ternary SNARE complex by favoring a largely open conformation of syntaxin-1A^{LE} (Wang et al., 2017). We tested the effect of the LE mutations on the configurations of the SNARE complex (Figure S8). While the syntaxin-1A^{LE} readily allows ternary SNARE complex formation starting from the Munc18-1 / syntaxin-1A^{LE} complex upon addition of synaptobrevin-2 and SNAP-25A in the absence of Munc13, it leads to mixtures of both parallel and anti-parallel syntaxin-1A / synaptobrevin-2 and syntaxin-1A / SNAP-25A subconfigurations (Figure S8) in the absence of Munc13. The syntaxin-1A^{LE} mutant therefore in principle allows one to decouple these two molecular functions of Munc13 *in vivo* since it bypasses one of the functions of Munc13, *i.e.*, the transit of syntaxin into the ternary SNARE complex, but not the proper assembly of the SNARE complex.

We next turned to experiments with autaptic Munc13-1/2 double deficient neurons that lack any synaptic responses. Overexpression of Munc13-1 or Munc13-2 rescues this phenotype with differential effects on short-term presynaptic plasticity (Rhee et al., 2002; Rosenmund et al., 2002; Varoqueaux et al., 2002). Here we show that overexpression of syntaxin-1A^{LE} in the Munc13-1/2 double-knockout neurons was able to restore some neurotransmission, with approximately 14% of neurons that overexpressed the syntaxin-1A^{LE} mutant exhibiting synaptic release (Figures 7A–C and 7E). Moreover, the evoked excitatory postsynaptic currents (EPSCs) were significantly decreased in those mutants compared to overexpression using wild-type Munc13-1 (Munc13-1; 4.5 ± 0.36 nA; syntaxin-1A^{LE} mutant; 0.05 ± 0.037 nA) (Figures 7D–E). We also observed a concomitant decrease in the size of the readily releasable pool (RRP), as assessed by the EPSC induced by the exogenous application of a hypertonic sucrose (0.5 M) solution (Munc13-1; 0.30 ± 0.051 nC; syntaxin-1A^{LE} mutant; 0.018 ± 0.0034 nC) (Figures 7D and 7F). We calculated an overall vesicle fusion probability as the ratio of the average EPSC amplitude to the RRP size (Figure 7G) and observed a decrease in vesicle fusion probability from $7.2 \pm 0.8\%$ for neurons expressing Munc13-1 to $4.0 \pm 1.2\%$ in syntaxin-1A^{LE} expressing neurons that showed responses.

Next, we examined short-term synaptic plasticity by measuring synaptic responses during low-frequency stimulation (trains of 13 stimuli delivered at 0.2 Hz; Figure 7H) and high-frequency stimulation (50 stimuli delivered at 10 Hz; Figure 7I). In both stimulation paradigms, we observed a strong progressive rundown of EPSC amplitudes. In some cases, the evoked EPSCs in the syntaxin-1A^{LE} mutant expressing neurons that showed responses were not sustained and disappeared entirely during high-frequency 10 Hz stimulation. Regardless of stimulation frequency, within 3–4 stimulations, vesicle fusion was largely depleted in syntaxin-1A^{LE} mutant neurons suggesting that a rapid depletion of release sites, or a severe deficit in synaptic vesicle priming or re-priming is produced by the loss of Munc13-1, or both.

We detected a significant reduction of mEPSC frequency for syntaxin-1A^{LE} mutant overexpression compared to Munc13-1 overexpression (Munc13-1: 1.56 ± 0.23 Hz; syntaxin-1A^{LE} mutant: 0.07 ± 0.002 Hz) but not amplitude (Munc13-1; 29.0 ± 2.96 pA; syntaxin-1A^{LE} mutant: 26.4 ± 5.30 pA) (Figures 7J–L), suggesting that the postsynaptic sensitivity to quantal release at single synapses was not changed but that the overall release probability was decreased. To confirm that the observed impairments in neurotransmission in syntaxin-1A^{LE} mutant neurons are due to problems relating to presynaptic fusion machinery, and not Ca²⁺ entry or action potential generation, we measured synaptic responses produced by the Ca²⁺ ionophore, calcimycin (Figure 7M–N). As expected, treatment with 100 μ M calcimycin also revealed a significant deficit in neurotransmission (Munc13-1 3.52 ± 0.49 nC compared to syntaxin-1A^{LE} 0.10 ± 0.047 nC). Together with a previous report that showed that the total number of synapses in Munc13-1/2 double-knockout and control neurons were identical (Varoqueaux et al., 2002; Imig et al., 2014), the overall reduction of synaptic neurotransmitter release by syntaxin-1A^{LE} mutant overexpression is likely due to an impairment of the synaptic vesicle machinery

DISCUSSION

Previous studies of Munc13 and Munc18 actions *in situ* have demonstrated a critical requirement of these proteins in neuron function. Knockout of either Munc13 or Munc18 results in near total loss of synaptic transmission (Augustin et al., 1999; Richmond et al., 1999; Verhage et al., 2000). However the lack of detailed structural information of the complex between Munc13, Munc18 and the SNARE complex, in combination with the severity of knockout studies, has hindered a detailed description of the molecular mechanisms of Munc13 or Munc18. Therefore, we turned to an *in vitro* approach using two techniques: single molecule FRET measurements and an *in vitro* single-vesicle fusion assay utilizing reconstituted proteins. Together, these techniques uncovered a new coordinated function of Munc13 and Munc18 as critical in not only the mere formation of the SNARE complex, but in the assembly of a SNARE complex in which all components are in proper relative orientation. Taken together, the consequences of Munc13 knockout go beyond its role in the transfer of syntaxin from Munc18 into the ternary SNARE complex, but also result in the generation of evoked-fusion incompetent, improperly assembled ternary SNARE complexes.

Munc13-1 has a molecular function that is independent of Munc18-1

We found that the MUN domain of Munc13-1 promotes the proper parallel subconfiguration between syntaxin-1A and synaptobrevin-2 when assembling the ternary SNARE complex starting from the syntaxin-1A / SNAP-25A complex (Figures 1B–F), *i.e.*, it prevents improper subconfigurations (Figure 1). Proper formation of the syntaxin-1A / synaptobrevin-2 subconfiguration has profound functional consequences: inclusion of the MUN domain in our single vesicle fusion assay approximately quadrupled the Ca²⁺-triggered amplitude and the fusion ratio (Figures 2C–E). This increase in Ca²⁺-triggered amplitude is due to the ability of the MUN domain to produce the proper syntaxin-1A / synaptobrevin-2 subconfiguration during ternary SNARE complex assembly rather than a direct role in fusion itself since removal of the MUN domain after SV-PM vesicle

association but prior to Ca^{2+} -triggering produced similar results to keeping the MUN domain present throughout stages (compare protocols “All” and “Pre” in Figure 2, Figure S3). Moreover, addition of the MUN domain only after SV-PM vesicle association had no effect whatsoever on fusion (protocol “Post” in Figure 2).

Inclusion of the longer C1C2BMUN or C1C2BMUNC2C fragments of Munc13-1 in the fusion assay enhanced the Ca^{2+} -triggered amplitude and fusion ratio in a manner similar to the MUN domain (Figures 3C–D). However, these longer fragments were able to achieve these effects at twenty and hundred fold lower concentrations than the MUN domain, respectively. This enhanced activity of these fragments is likely due to increased binding to the PM vesicle membrane via its C1 and C2B domains (Figure S6). Inclusion of the C2C domain in the Munc13 fragment (*i.e.*, C1C2BMUNC2C) further lowered the concentration of the Munc13 fragment that was required to maximize the effect on the Ca^{2+} -triggered fusion amplitude by a factor of ~ 5 (Figure 3C) likely through an increased synaptic vesicle association via the C2C domain (Figure S5). Together the C1, C2B and C2C domains act by effectively increasing the local concentration of the MUN domain near synaptic fusion sites.

Electron cryo-tomography studies revealed that nearly all associated SV-PM vesicle pairs fused upon Ca^{2+} -addition within 1 min (Gipson et al., 2017). Moreover, the lack of C1C2BMUN fragments at a considerable number of contact sites before Ca^{2+} addition is consistent with the notion that Munc13 catalyzed proper SNARE complex assembly and then dissociated from some of the primed pre-fusion complexes, prior to Ca^{2+} triggering.

Cooperation of Munc13-1 with Munc18-1

In addition to its autonomous function of promoting the proper syntaxin-1A / synaptobrevin-2 subconfiguration, the MUN domain also cooperates with Munc18-1 to promote the proper syntaxin-1A / SNAP-25A subconfiguration within the assembled ternary SNARE complex (Figures 4E–H). Thus, while the MUN domain alone is sufficient to promote the proper syntaxin-1A / synaptobrevin-2 subconfiguration starting from the syntaxin-1A / SNAP-25A complex (Figures 1D–F) and consequently increasing the Ca^{2+} -triggered fusion amplitude (Figure 3), the proper syntaxin-1A / SNAP-25A subconfiguration is only achieved when starting from the syntaxin-1A / Munc18-1 complex. Indeed, we observed a substantially improved Ca^{2+} -sensitivity when both Munc13-1 and Munc18-1 are included (compare Figure 3F and Figure 6G).

Taken together, Munc13-1 and Munc18-1 are factors for establishing the proper subconfigurations during *trans* ternary SNARE complex assembly (with parallel arrangements of the SNARE components and 1:1:1 stoichiometry) by suppressing improper subconfigurations, *i.e.*, they promote proper ternary SNARE complex assembly (Figure 8). The cooperation of Munc18-1 and Munc13-1 in promoting the proper SNARE complex assembly suggests that Munc18-1 has an indirect, but essential role in achieving high fusion efficiency, perhaps explaining the severe phenotype of deletion of Munc18-1 in neurons (Verhage et al., 2000).

The existence of factors for proper assembly of ternary SNARE complex may be a general phenomenon since in the context of a different SNARE-mediated fusion process, the so-

called HOPS complex, these factors are essential in promoting maximum efficiency of homotypic vacuolar fusion (Zick and Wickner, 2014). However, while there is a Munc18-1 homolog in the HOPS complex (Vps33) and it has an effect on ternary SNARE complex formation as suggested by structural studies (Baker et al., 2015), there is no Munc13-1 homolog. These findings suggest that evolution of Ca^{2+} -triggered fusion machineries deviated from that of constitutive homotypic membrane fusion. In support of this notion, all Munc13 homologues are thought to be involved in Ca^{2+} -triggered exocytosis (Koch et al., 2000; Lipstein et al., 2012).

Overexpression of the syntaxin-1A^{LE} mutant in Munc13-1/2 deficient mice

The syntaxin-1A^{LE} mutant promotes ternary SNARE complex formation in the absence of Munc13, but it is unable to promote the proper subconfigurations of the components of the SNARE complex (Figure S8). In further support of the newly discovered molecular function of Munc13, we performed overexpression experiments with either Munc13-1 or the constitutively open mutant of syntaxin-1A^{LE} mutant in neuronal cultures from Munc13-1/2 deficient mice. The arrest of release in Munc13-1/2 double-knockout mice was only minimally restored when syntaxin-1A^{LE} was expressed (Figure 7).

Molecular mechanisms of priming by Munc13-1 and Munc18-1

When some of the SNARE complexes around the contact site between the synaptic and plasma membranes are improperly assembled in the absence of Munc13, they have a large effect on morphologies of the contact sites between SV and PM vesicles (Gipson et al., 2017). Upon inclusion of Munc13, the contacts are largely restricted to point contacts only, *i.e.*, no long contacts are present and very few “dead-end” hemifusion diaphragms were observed prior to Ca^{2+} -addition. The ternary SNARE complex interacts with both synaptotagmin-1 and with complexin-1, forming a primed and “locked” complex (Zhou et al., 2015, 2017) that is required for maximum probability of Ca^{2+} -triggered release. These interactions will not occur if there are improper subconfigurations within the ternary SNARE complex. In particular, an anti-parallel subconfiguration between syntaxin-1A and synaptobrevin-2 would prevent formation of the SNARE / complexin-1 / synaptotagmin-1 tripartite interface (Zhou et al., 2017). Moreover, an anti-parallel subconfiguration between SNAP-25A and syntaxin-1A would prevent formation of the primary interface between synaptotagmin-1 and the ternary SNARE complex since it involves the SNAP-25A and syntaxin-1A components of the SNARE complex (Zhou et al., 2015). This model explains why there is a further substantial increase in Ca^{2+} -sensitivity upon inclusion of Munc13 and Munc18 *in vitro* (Figures 3 and 6). Multiple SNARE complexes may be cooperating to achieve maximum speed and efficiency of Ca^{2+} -triggered fusion. If such assemblies included improperly assembled SNARE complexes, they would lose cooperativity and thus fail to maximally evoke fusion upon Ca^{2+} -triggering while suppressing Ca^{2+} -independent fusion. This is indeed what we observe: the MUN domain mediated assembly of proper SNARE complex by a factor of 1.6 (Figure 1F), while increasing the Ca^{2+} -triggered amplitude by a factor of 3.6 (Figure 2C), suggesting a cooperative process.

Conclusions

The role of Munc13-1 in short-term plasticity may be related to both molecular functions of Munc13-1 since the amount of properly assembled SNARE complex will depend on the effective concentration of the MUN domain, which may in turn be subject to regulation by the other domains of Munc13-1, including its calmodulin binding domain. Ca^{2+} -binding to the C2B domain, the synergy between C1, C2B, and C2C domains (Liu et al., 2016), and the Ca^{2+} -dependent interaction between calmodulin and Munc13 (Junge et al., 2004) may localize Munc13 to sites of docked synaptic vesicles and increase its ability to assist in proper SNARE complex assembly, as corroborated by the concentration dependence of the various Munc13 fragments in our fusion experiments (Figures 3C–E). Indeed, mutations of the Munc13-2 C2B domain affect neurotransmitter release upon a single action potential as well as short-term synaptic plasticity (Shin et al., 2010) and mutations in the interface regions between the C1, C2B and MUN domains have differential effects on evoked release and the readily releasable pool (Xu et al., 2017), suggesting that the two molecular functions of Munc13 may be differentially regulated in the neuron. It is of course possible that Munc13 has a more direct role in the fusion process although our fusion experiments suggest that Munc13 can be removed after proper assembly and prior to Ca^{2+} -triggering without a significant effect on Ca^{2+} -triggered fusion. Taken together, regulation of presynaptic plasticity via Munc13 may be in part accomplished by its profound molecular function on ensuring proper assembly of the ternary SNARE complex.

Experimental Procedures

See STAR Methods.

STAR Methods

Contact for Reagent and Resource Sharing

Further information and requests for resources and reagents should be directed to and will be fulfilled by the Lead Contact, Axel T. Brunger (brunger@stanford.edu).

Experimental Model and Subject Details

Animals—Mouse lines, age: DIV10–15, the sex for the cultures were not distinguished.

Generation of Munc13-1/2 DKO mice and mouse breeding—Mouse breeding was done with permission of the Niedersächsisches Landesamt für Verbraucherschutz und Lebensmittelsicherheit (LAVES; 33.19.42502-04-15/1817). All animals were kept according to the European Union Directive 63/2010/EU and ETS 123 in individually ventilated cages (IVCs) under specific pathogen-free conditions at $21 \pm 1^\circ\text{C}$ and $55\% \pm 10\%$ relative humidity. The light/dark cycle was 12 h/12 hr. Mice were group-housed in IVCs type I superlong (435 cm² floor area; TECHNIPLAST). The mouse environment consisted of food and tap water ad libitum, bedding, and nesting material. Cages were changed once a week. The animal health status was controlled daily by animal caretakers as well as by a veterinarian. Systematic health monitoring was carried out quarterly according to FELASA recommendations with either NMRI sentinel mice or animals directly taken from the colony. Health monitoring consisted of serological analyses and microbiological, parasitological,

and pathological examinations. The mouse colony used for experiments did not exhibit signs of the pathogens routinely tested for. Mice lacking Munc13-1 (Unc13A) and Munc13-2 (Unc13B) (Augustin et al., 1999; Varoqueaux et al., 2002) were initially generated using 129/ola embryonic stem cells. Since the establishment of the initial M13-DKO line, the line has been bred into the C57BL/6N background more than 10 times. As the remaining 129/ola genetic contribution has not been assessed in the M13-DKO colony, the line must be regarded to be on a mixed C57BL/6N;129/ola background, with a minimal 129/ola contribution. M13-DKO and CTR littermates, obtained by interbreeding Unc13A+/-;Unc13B+/- and Unc13A+/-;Unc13B-/- mice, were used for all experiments. CTRs with genotypes Unc13A+/+;Unc13B-/-, Unc13A+/+;Unc13B+/- and Unc13A+/-;Unc13B+/- show no obvious changes in brain morphology or cage behavior, and cultured neurons and hippocampal slices of mice with these genotypes show essentially normal transmitter release (Varoqueaux et al., 2002; Breustedt et al., 2010). The gender of animals used for experimentation was not checked because all previous studies on M13-DKOs had indicated that the gender does not affect the M13 DKO phenotype.

Methods Details

Protein expression and purification—We used the same constructs and protocols to purify cysteine-free SNAP-25A, synaptotagmin-1, complexin-1 as described in ref. (Lai et al., 2014). For syntaxin-1A and synaptobrevin-2 we used the hexa-histidine tagged constructs and protocol described in ref. (Lai et al., 2016). The protein sample concentrations were measured by UV absorption at 280 nm, aliquots were flash frozen in liquid nitrogen and stored at -80°C . Munc18-1a was expressed in BL21(DE3) cells using 0.5mM IPTG for 12–16 hours at 20°C from a pPROExHTa vector (Invitrogen, Carlsbad, CA) as an N-terminal hexa-histidine tag with a tobacco etch virus (TEV) protease cleavage site to remove the tag. Cells from 6 liters of induced culture were re-suspended in 200 mL of buffer A (20 mM sodium phosphate pH 8, 300 mM NaCl, 10 mM imidazole) containing 1 mM PMSF and 4 EDTA free protease inhibitor tablets (Roche, Basel, Switzerland). Cells were lysed by three passes through the Emulsiflex C5 homogenizer (Avestin, Ottawa, Canada) at 15000 psi. Lysate was clarified by centrifugation in the Ti45 rotor (Beckman Coulter, Brea, CA) for 35 minutes at 40,000 RPM. The supernatant was bound to 5 mL of Nickel NTA beads (Qiagen, Hilden, Germany) for 30 minutes with stirring at 4°C . The beads were harvested by centrifugation, poured into a column, attached to the Akta prime (GE Healthcare, Uppsala, Sweden) and washed with 60 mL of buffer A supplemented with 50mM Imidazole. Munc18a was eluted with buffer A supplemented with 300mM Imidazole. Protein containing fractions were combined, 70ug of TEV protease was added to cleave the tag and the mixture was dialyzed against 1 liter of 20 mM Tris pH 8, 50 mM NaCl, 1 mM EDTA, 5 mM DTT (monoQ buffer A) at 4°C overnight. Any precipitate was removed from the dialyzed sample by centrifugation and the supernatant was injected on the monoQ column (GE Healthcare, Uppsala, Sweden) equilibrated in monoQ buffer A. The column was washed with 25 column volumes of monoQ buffer A and then eluted using a linear NaCl gradient from 50 to 500 mM NaCl over 30 column volumes. Protein containing fractions were combined and dialyzed against 1 liter of 20 mM HEPES pH 7.5, 180 mM NaCl, 20 μM EGTA, 0.1% 2-mercaptoethanol. The protein concentration was measured by absorption at 280 nm and aliquots were flash frozen in liquid nitrogen and stored at -80°C .

The MUN domain (amino acid range 859–1531, excluding residues 1408–1452) was cloned into a N-terminal hexa-histidine TEV cleavable construct and was expressed in BL21 *E. coli* and grown in 2L of TB. The deletion in this construct prevents aggregation (Ma et al., 2013). The cells were IPTG induced at OD 0.6–0.8 and grown for at least 12 hours at 25 °C. The cells were collected by centrifuging the solution in a JA-14 rotor (Beckman Coulter) at 10,000 rpm for 10 minutes. The cells were resuspended and homogenized in a lysis buffer composed of 20 mM Tris, pH 8.5, 300 mM NaCl, 2 mM DTT, 10% glycerol, 1 mM PMSF, and supplemented with EDTA-free protease inhibitor tablets (Roche Applied Science). The cells were lysed by sonication using a Sonicator ultrasonic processor XL (Misonix Corporation) with the following program: 3 seconds on, 8 seconds off, for 10 minutes at power 8.5. The cell lysate was then centrifuged at 40,000 for 1 hour in a Ti-45 rotor (Beckman Coulter). The supernatant was then applied to 5 mL bed volume of Ni-NTA-agarose column (Qiagen) for 2 hours stirring at 4°C. The column was washed with the lysis buffer, then the protein was eluted using 50 mM Tris, pH 8.5, 300 mM NaCl, 400 mM imidazole, 0.5 mM DTT, and 10% glycerol. The elution was then collected into a 10,000 molecular mass cut off SnakeSkin Dialysis Tubing (Thermo Scientific), a 50 µL aliquot of TEV at 48 mg/mL was added, and placed in dialysis buffer of consisting of 20 mM Tris, pH 8.5, 50 mM NaCl, 0.5 mM DTT, and 10% glycerol overnight at 4 °C. The cleaved protein solution was applied to a MonoQ 4.6/100 ion exchange column (GE Healthcare) equilibrated with 20 mM Tris, pH 8.5, 50 mM NaCl, 1 mM DTT, 10% glycerol (MonoQ buffer A). The protein was eluted with 20 mM Tris, pH 8.5, 1 M NaCl, 1 mM DTT, 10% glycerol using a linear gradient from 50 mM NaCl to 1 M NaCl over 30 column volumes. The appropriate fractions were pooled and applied to a HiLoad Superdex 200 16/60 PG size exclusion column (GE Healthcare) equilibrated in 20 mM Tris, pH 8.5, 150 mM NaCl, 10% glycerol, and 5 mM DTT (Superdex buffer). The protein containing fractions were pooled and concentrated, the protein concentration was measured by UV absorption at 280 nm, and aliquots were flash frozen in liquid Nitrogen and stored at –80 °C.

The C1C2BMUN fragment (amino acid range 529–1531, excluding residues 1408–1452) was cloned into a pFastBac HTB vector with an N-terminal hexa-histidine tag and a TEV cleavage site, as described in ref. (Ma et al., 2013). Cells from 8L of SF9 cell culture were re-suspended in 300 mL re-suspension buffer (RB) (50 mM Tris, pH 8.0, 250 mM NaCl, 10 mM imidazole, 1 mM TCEP) containing 6 EDTA-free protease inhibitor tablets (Roche Applied Science). The cells were lysed via 3 passes through the Avestin C5 homogenizer at 15000 psi. The lysate was clarified by centrifugation for 1 hour at 40,000 RPM in the Ti45 rotor (Beckman). The supernatant was mixed with 8 mL Ni-NTA beads (Qiagen) at 4 °C stirring for 1 hour. The beads were washed using an Akta Prime system (GE Healthcare) with 50 mL each of RB, RB + 1% triton X-100, RB + 750 mM NaCl, RB, then eluted with RB + 300 mM imidazole. Peak fractions were pooled and then 200 µL of 11 mg/mL TEV protease, and glycerol to 10% (w/v) was added. The mixture was dialyzed overnight against 1L of 20 mM Tris, pH 8.0, 0.5 mM TCEP, 50 mM NaCl, 10% glycerol. The TEV cleaved protein was injected on a monoQ 4.6/100 column (GE healthcare) equilibrated in 20 mM Tris, pH 8.0, 50 mM NaCl, 0.5 mM TCEP, 10% glycerol. The column was washed with 20 column volumes of the equilibration buffer and eluted with a NaCl gradient to 500 mM over 30 column volumes. Peak fractions were combined and the protein concentration was

measured by UV absorption at 280 nm. Aliquots of 100 μ L were flash frozen in liquid N₂ and stored at -80°C .

The C1C2BMUNC2C fragment (amino acid range 529–1735, excluding residues 1408–1452) was cloned into a pFASTBAC vector with a N-terminal GST tag and a TEV cleavage site, as described in (Liu et al., 2016). Cells from 4 L of SF9 cell culture were re-suspended in 300 mL re-suspension buffer (RB) (50 mM Tris, pH 8.0, 250 mM NaCl, 1 mM TCEP, 10% (w/v) glycerol) containing 6 EDTA-free protease inhibitor tablets (Roche Applied Science) and 10 mM imidazole. The cells were lysed via 3 passes through the Avestin C5 homogenizer at 15000 psi. The lysate was clarified by centrifugation for 1 hour at 40,000 RPM in the Ti45 rotor (Beckman). The supernatant was mixed with 10 mL of glutathione sepharose 4b (GE Healthcare) at 4°C stirring for 2 hours. The beads were washed using an Akta Start system (GE Healthcare) with 80 mL each of RB, RB + 1% Triton X-100, RB + 750 mM NaCl, RB, then eluted with RB + 20mM reduced Glutathione. Peak fractions were pooled and 100 μ L of 11 mg/mL TEV protease was added to remove the GST. The protein was concentrated using a 50 kDa Molecular Weight cutoff filter (Millipore) to 5 mL and injected on a superdex 200 16/60 column (GE Healthcare). Peak fractions were combined and the protein concentration was measured by UV absorption at 280 nm. Aliquots of 200 μ L were flash frozen in liquid N₂ and stored at -80°C .

Chinese hamster NSF with a TEV cleavable N-terminal hexa-histidine tag was expressed from pPROEX-1 in *E.coli*. BL21 (DE3) RIL cells (Agilent Technologies). After lysis and clarification, the lysate was loaded onto a 5 mL Ni-NTA agarose column (Qiagen), washed with 50 mL of 50 mM Tris, pH 8.0, 300 mM NaCl, 60 mM imidazole, and eluted in the wash buffer supplemented with 350 mM imidazole. Fractions containing NSF were pooled and supplemented with 1 mM EDTA, 1 mM ATP, and 10% glycerol. TEV protease was added to pooled fractions, and the sample was left at 4°C overnight. The protein was then concentrated using an Amicon Ultra-15 centrifugal filter with 100-kDa molecular mass cut off (Millipore) to reduce the volume, and run through a Superdex 200 16/600 size exclusion column (GE Healthcare) that was equilibrated with 50 mM Tris, pH 8.0, 150 mM NaCl, 10% glycerol, 1 mM EDTA, 1 mM ATP, and 1 mM DTT. The protein containing fractions were pooled and concentrated, the protein concentration was measured by UV absorption at 280 nm, and aliquots were flash frozen and stored at -80°C .

Rat α SNAP was expressed with an N-terminal TEV cleavable decahistidine tag from a codon-optimized plasmid using the pJexpress414 backbone (DNA 2.0) in *E.coli*. BL21 (DE3) cells. The clarified lysate was loaded onto a 5 mL Ni-NTA agarose column, washed with 50 mL of 50 mM Tris, pH 8.0, 300 mM NaCl, 60 mM imidazole, and eluted in the wash buffer supplemented with 350 mM imidazole. TEV protease was added to pooled fractions, and the sample was left at 4°C overnight. The protein was then run through a Superdex 200 16/600 size exclusion column that was equilibrated with 50 mM Tris, pH 8.0, 150 mM NaCl, and 0.5 mM TCEP. The protein containing fractions were pooled and concentrated, the protein concentration was measured by UV absorption at 280 nm, and aliquots were flash frozen and stored at -80°C .

For the cytoplasmic domains of syntaxin-1A, synaptobrevin-2, and of SNAP-25A used for single molecule experiments, all constructs were cloned into a pTEV5 vector with an N-terminal TEV cleavable hexa-histidine tag. The cytoplasmic domain of rat syntaxin-1A (amino acid range 1–265) (used in Figures 1, 4, 5 and S8) and the cytoplasmic domain of synaptobrevin-2 (used in Figure S1) were fused to a C-terminal biotinylation sequence (GLNDIFEAQKIEWHE) and co-expressed with the BirA gene engineered in pACYC184 (Avidity) to perform *in vivo* biotinylation. The construct for the cytoplasmic domain of the syntaxin-1A^{LE} mutant (L165A/E166A) was obtained from the construct of the cytoplasmic domain of syntaxin-1A using the QuickChange Kit (Agilent). Cells were grown to OD600 of about 0.8 at 37 °C, and then induced with 0.5 mM IPTG at 30 °C in the presence of 0.1 mM biotin for 4 hours. SNAP-25A (amino acid range 1–206) and the cytoplasmic domain of synaptobrevin-2 (amino acid range 1–96) were expressed in *E. coli* (DE3) by growing the cells to an OD600 of about 0.8 at 37 °C, then induced with 0.5 mM IPTG at 30 °C for 4 hours. All proteins were purified by resuspending the cell pellets from a 1 L of culture in PBS (50 mM NaH₂PO₄, pH 8.0, 300 mM NaCl, 0.5 mM DTT) buffer supplemented with 0.5 mM PMSF and EDTA-free Complete Protease Inhibitor Cocktail tablets (Roche Applied Science). Cells were lysed by sonication and inclusion bodies were spun down by centrifugation at 20,000 rpm for 30 minutes. The supernatant was bound to Nickel-NTA agarose beads (Qiagen) to remove impurities by washing extensively with PBS containing 20 mM imidazole. Proteins were eluted with PBS containing 400 mM imidazole. 100 µg of TEV was added to cleave off the N-terminal hexa-histidine tags and dialyzed overnight in 20 mM Tris, pH 8.0, 50 mM NaCl, 0.5 mM EDTA, 1 mM DTT. The free TEV protease and the cleaved proteins were separated and concentrated on a 1 mL HiTrap Q column (GE Healthcare) with a linear gradient of 0.05 to 0.6 M NaCl in 20 mM Tris, pH 7.5, 0.5 mM TCEP. The cytoplasmic domain of synaptobrevin-2 (amino acid range 1–96) does not bind to ion exchange columns, so instead we concentrated the sample and purified it using a Superdex 75 size exclusion column (GE Healthcare) in 20 mM Tris, pH 7.5, 150 mM NaCl, 0.5 mM TCEP. The protein purity was checked using SDS-PAGE gel electrophoresis (>95%). The protein concentration was measured by UV absorption at 280 nm.

Proteins labeling—Protein labeling for the single molecule experiments in Figures 1, 4, 5, S1, S3, and S8, was performed by starting with a cysteine-free template and generating single cysteine mutations using QuickChange Kit (Agilent) at surface exposed positions based on the available crystal structures. Labeling sites used in this work are: syntaxin-1A E35C, syntaxin-1A S193C, syntaxin-1A S249C, SNAP-25A K76C, synaptobrevin-2 A72C, and synaptobrevin-2 A82C. Proteins were labeled with the fluorescent dyes Alexa 488 C₅, Alexa 555 C₂, or Alexa 647 C₂ Maleimide (Thermo Fisher Scientific Inc.) in TBS overnight on a rotating platform at 4 °C. The MUN domain was labeled at the primary amino group (-NH₂) at the N-terminus with the fluorescent dye Alexa 555 NHS Ester (Thermo Fisher Scientific Inc.) in 50 mM NaH₂PO₄, pH 6.5, 150 mM NaCl, 0.5 mM TCEP. Labeled proteins were separated from free dye by a column packed with Sephadex G50 resin in 20 mM Tris, pH 7.5, 150 mM NaCl, 0.5 mM TCEP (GE Healthcare).

Instrument setup—All single vesicle fusion and single molecule experiments were performed on a prism-type total internal reflection fluorescence (TIRF) microscope using

532 nm (green) laser (CrystaLaser) excitation. Two observation channels were created by a 640 nm single-edge dichroic beamsplitter (FF640-FDi01-25x36, Shemrock): one channel was used for the fluorescence emission intensity of the content dyes or the Alexa 555 dye and the other channel for that of the Cy5 dye that are part of the injected Ca^{2+} -solution or the Alexa 647 dye. The two channels were recorded on two adjacent rectangular areas ($45 \times 90 \mu\text{m}^2$) of a charge-coupled device (CCD) camera (iXon+ DV 897E, Andor Technology USA, South Windsor CT). The imaging data were recorded with the smCamera program (Taekjip Ha, Johns Hopkins University, Baltimore).

Flow chambers were assembled by creating a “sandwich” consisting of a quartz slide and a glass coverslip that were both coated with polyethylene glycol (PEG) molecules consisting 0.1 % (w/v) biotinylated-PEG except when stated otherwise, and using double-sided tape to create up to five flow-chambers.

Single molecule experiments—For the experiments described in Figures 1 and 4, the biotinylated and Alexa 647 labeled cytoplasmic domain of syntaxin-1A was tethered to biotinylated-PEG surface, using 0.1 mg/mL streptavidin and conditions that produced a density of about 1000 syntaxin-1A molecules per $45 \times 90 \mu\text{m}^2$ field of view, followed by buffer wash with TBS (20 mM Tris, pH 7.5, 150 mM NaCl). To assess the uniformity and consistency of the coverage of surface-tethered syntaxin-1A, we counted spots representing surface-tethered syntaxin-1A molecules in three individual frames of data acquisition movies from each of the chambers, which were used to analyze the density of surface-tethered syntaxin-1A between chamber to chamber on the same microscope slide. We found that the tethered syntaxin-1A surface coverage was consistent and reproducible.

For the incorporation experiments shown in Figures 1C, 1H, 4B, 4F and S8B, unlabeled syntaxin-1A at the same dilution was used in order to avoid FRET from the donor labels attached to labels attached to syntaxin-1A that were added in solution. Each set of experiments that is shown in the same bar chart (Figures 1C, 1H, 4B, 4F and S8B) was performed on the same microscope slide but in different chambers. The consistency and reproducibility of the syntaxin-1A surface coverage enables comparison of counts of molecules.

For the experiments described in Figures 1A–F, we formed the initial syntaxin-1A / SNAP-25A complex by incubating 1 μM SNAP-25A for 5 minutes to surface-tethered syntaxin-1A, followed by removal of unbound proteins by rinsing with TBS (20 mM Tris, pH 7.5, 150 mM NaCl). Subsequently, the surface-tethered syntaxin-1A / SNAP-25A complex was incubated with 1 nM synaptobrevin-2 that was labeled at residue 82 with FRET donor dye Alexa 555, and the MUN domain at the specified concentration or BSA control for 5 minutes. Unbound proteins were subsequently washed away by rinsing three times with 200 μL TBS. To measure the degree of incorporation of synaptobrevin-2 into ternary SNARE complexes, we counted the number of spots arising from Alexa 555 dye labeled synaptobrevin-2 molecules. To measure FRET efficiency between labels attached to syntaxin-1A and synaptobrevin-2, syntaxin-1A was labeled with FRET acceptor dye (Alexa 647) at residue 249 prior to surface-tethering.

For the experiments described in Figures 1G–K, we incubated surfaced-tethered syntaxin-1A with 1 nM SNAP-25A that was labeled with FRET donor dye Alexa 555 at residue 76, 1 μ M synaptobrevin-2, and the MUN domain at the specified concentration or BSA control for 5 minutes. Note that we used a higher concentration of synaptobrevin-2 in these experiments than in the experiments shown in Figures 1A–F in order to increase the yield of ternary SNARE complex formation. Unbound proteins were subsequently washed away by rinsing three times with 200 μ L TBS. Experiments to measure the incorporation of SNAP-25A molecules into ternary complex, and for measuring smFRET efficiency between labels attached to SNAP-25A and syntaxin-1A were performed with the specified labels, using the same procedures as in the experiments described for Figures 1A–F above.

For the experiments described in Figures 4A–D, we formed the initial syntaxin-1A / Munc18-1 complex by incubating 1 μ M Munc18-1 for 5 minutes to the surface-tethered syntaxin-1A, followed by removal of unbound proteins by washing with TBS. To form ternary SNARE complex, we incubated the surface-tethered syntaxin-1A / Munc18-1 complex with 10 nM synaptobrevin-2 that was labeled with FRET donor dye (Alexa 555) at residue 82, 1 μ M SNAP-25A, and the MUN domain at the specified concentration or BSA control. The concentration of labeled synaptobrevin-2 (10 nM) produced a sufficient amount of ternary SNARE complex. Unbound proteins were subsequently washed away by rinsing three times with 200 μ L TBS. Experiments to measure the incorporation of synaptobrevin-2 molecules into ternary complex, and for measuring smFRET efficiency between labels attached to synaptobrevin-2 and syntaxin-1A were performed with the specified labels, using the same procedures as in the experiments described for Figures 1A–F above.

For the experiments described in Figures 4E–H, we formed the initial syntaxin-1A / Munc18-1 complex by incubating 1 μ M Munc18-1 for 5 minutes to the surface-tethered syntaxin-1A, followed by removal of unbound proteins by washing with TBS. To form ternary SNARE complex, we incubated the surface-tethered syntaxin-1A / Munc18-1 complex with 1 μ M synaptobrevin-2, 10 nM SNAP-25A that was labeled with FRET donor dye (Alexa 555) at residue 76, and the MUN domain at the specified concentration or BSA control. The concentration of labeled SNAP-25A (10 nM) produced a sufficient amount of ternary SNARE complex. Unbound proteins were subsequently washed away by rinsing three times with 200 μ L TBS. Experiments to measure the incorporation of SNAP-25A molecules into ternary complex, and for measuring smFRET efficiency between labels attached to SNAP-25A and syntaxin-1A were performed with the specified labels, using the same procedures as in the experiments described for Figures 1G–K above.

For the experiments described in Figures S8A–E, we formed the initial syntaxin-1A^{LE} / Munc18-1 complex by incubating 1 μ M Munc18-1 for 5 minutes to the surface-tethered syntaxin-1A^{LE}, followed by removal of unbound proteins by washing with TBS. To form ternary SNARE complex, we incubated the surface-tethered syntaxin-1A^{LE} / Munc18-1 complex with 1 μ M SNAP-25A and 10 nM synaptobrevin-2 that was labeled with FRET donor dye (Alexa 555) at residue 82 (top panel) or with 1 μ M synaptobrevin-2 and 10 nM SNAP-25A that was labeled with FRET donor dye (Alexa 555) at residue 76 (bottom panel). Unbound proteins were subsequently washed away by rinsing three times with 200 μ L TBS. Experiments to measure the incorporation of SNAP-25A and synaptobrevin-2 molecules

into ternary complex, and for measuring smFRET efficiency between labels attached to syntaxin-1A and synaptobrevin-2 or syntaxin-1A and SNAP-25A were performed with the specified labels, using the same procedures as in the experiments described for Figures 1A–K above.

Since extensive washing with protein-free buffer was performed after ternary SNARE complex assembly, it is unlikely that the MUN domain remains bound to the assembled SNARE complex. Thus, the observed differences in smFRET histograms in Figures 1E, 1J, 4C, and 4G are due to genuine differences between SNARE complexes, and not due to effects caused by affecting the conformational space of the fluorescent dyes that were attached to the specific labeling sites.

For the experiments described in Figure 5, we used 50 nm egg phosphatidylcholine (PC) liposomes (Avanti Polar Lipids) to passivate a surface coated with 1 mg/mL biotinylated BSA in order to create an environment surrounded by lipid bilayers (Choi et al., 2012). We used this method instead of a PEG-coated surface in order to maximize the efficiency of the disassembly process with NSF / α SNAP since a lipid bilayer increases the activity of α SNAP (Winter et al., 2009). The cytoplasmic domain of syntaxin-1A was stochastically labeled with Alexa 555 and Alexa 647 dyes at residues 35 and 249 and surface-tethered to a biotinylated BSA surface surrounded by a lipid bilayer through biotin-streptavidin linkage using 0.1 mg/mL streptavidin and conditions that produced a density of about 200–300 syntaxin-1A molecules per $45 \times 90 \mu\text{m}^2$ field of view, followed by buffer wash with TBS (20 mM Tris, pH 7.5, 150 mM NaCl). To determine the conformation of syntaxin-1A / SNAP-25A and syntaxin-1A / Munc18-1 complex, 1 μM of SNAP-25A or Munc18-1 was incubated for 5 minutes to surface-tethered syntaxin-1A and then washed with TBS to remove free proteins that did not form complex (Figures 5A and 5D). The selected FRET labeling pair of syntaxin-1A residues has an estimated α -carbon-to- α -carbon (C α -C α) distance of 2.7 nm based on the crystal structure of the syntaxin-1A / Munc18-1 complex (Misura et al., 2000), and is thus expected to produce high FRET efficiency in the closed state of syntaxin-1A when bound to Munc18-1. To form syntaxin-1A / Munc18-1 complex starting from the syntaxin-1A / SNAP-25A complex, we used the disassembling factors (1 μM NSF, 10 μM α SNAP, 1 mM ATP, 1 mM Mg^{2+}) in presence of 1 μM Munc18-1 (Figures 5B and 5E). We performed bulk steady-state fluorescence anisotropy measurements to confirm that the changes in the smFRET efficiencies are due to conformational changes of syntaxin-1A, and not due to effects caused by affecting the conformational space of the fluorescent dyes that were attached to the specific labeling sites. The steady-state anisotropy was measured with a Fluorolog spectrofluorometer (HORIBA scientific) relative to free Alexa 555 and 647 using an integration time of 2 seconds. The intramolecular FRET label sites of syntaxin-1A (residues 35 and 249) were labeled with either Alexa 555 or Alexa 647 dyes. For syntaxin-1A doubly labeled with Alexa 555, we used an excitation wavelength of 532 ± 5 nm and an emission wavelength of 575 ± 5 nm. For syntaxin-1A doubly labeled with Alexa 647, we used an excitation wavelength of 651 ± 5 nm and an emission wavelength of 671 ± 5 nm. The absorbance value for both dye labeled samples at the respective excitation wavelengths were adjusted to 0.05 AU to perform steady-state anisotropy measurements. The fluorescence anisotropy experiments (Table S6) suggest that

the orientations of dyes attached to syntaxin-1A residues 35 or 249 are not affected by the presence of SNAP-25A, Munc18-1, or the disassembly factors (NSF, α SNAP, ATP, $MgCl_2$).

Stoichiometry of SNARE complexes in the single molecule experiments—For the stoichiometry of tethered SNARE complexes in single molecule experiments, as mentioned above, the cytoplasmic domain of syntaxin-1A was tethered to the biotinylated-PEG surface at tens of picomolar concentration. To corroborate the notion that at most one syntaxin-1A molecule is incorporated in each individual complex analyzed in the single molecule experiments shown in Figures 1, 4, 5 and S8 we analyzed all single molecule fluorescence intensity time traces involving acceptor dye (Alexa 647) labeled syntaxin-1A (representative examples are shown in Figures 1D and 1I). The traces that exhibit a stepwise disappearance of the acceptor fluorescence intensity due to photobleaching of the dye molecule show a corresponding anti-correlated rise of the donor fluorescence intensity. This implies that there is exactly one acceptor dye in each analyzed fluorescent spot. We determined the acceptor dye labeling efficiency of the cytoplasmic domain of syntaxin-1A by measuring the absorbance of the labeled protein at 280 nm (corresponding to the protein concentration) and 647 nm (corresponding to the dye concentration) using a Nanodrop-1000 Spectrophotometer (NanoDrop Technologies). The ratio of the two measurements was used to estimate the labeling efficiency, yielding 87 %. Thus, all fluorescent spots most likely contain exactly one syntain-1A molecule.

To probe the number of SNAP-25A molecules in the observed single complexes, we incubated surface-tethered (unlabeled) syntaxin-1A with an equimolar mixture of 1 nM Alexa 555 labeled SNAP-25A (residue 76) and Alexa 647 labeled SNAP-25A (residue 76), along with 1 μ M cytoplasmic domain of synaptobrevin-2. We observed the fluorescence intensity of the Alexa 555 and Alexa 647 dyes in the field of view, and found that only 1.5 ± 0.7 are co-localized, implying that in all likelihood only one SNAP-25A molecule is involved in an individual complex observed in the single molecule experiments shown in Figures 1, 4, 5 and S8.

For the experiments with labeled synaptobrevin-2 (Figures 1A–F, 4A–D and S8A–E), a synaptobrevin-2 molecule is included in each observed complex, by definition. In the experiments with unlabeled synaptobrevin-2 (Figure 1G–K, 4E–H and S8A–E), synaptobrevin-2 is applied at 1000 fold excess concentration over SNAP-25A, and thus in all likelihood, all complexes that are observed in these experiments include at least 1 synaptobrevin-2 molecule.

Variable stoichiometries occur when SNAREs are mixed in solution in addition to the 1:1:1 syntaxin-1A / SNAP-25A / synaptobrevin-2 complex, *e.g.*, a 2:1 syntaxin-1A / SNAP-25A complex (Brunger, 2006). However, no complexes have been observed with more than one synaptobrevin-2 molecule. Taking into account that our tethered single molecule setup produces isolated syntaxin-1A molecules and single SNAP-25A in each individual complex, all complexes that are observed in the single molecule experiments shown in Figures 1, 4 and 5 most likely have 1:1:1 stoichiometry.

Fluorescence anisotropy binding assays—For the fluorescence binding experiments described in Figures S1A–C, the biotinylated and labeled (fluorescent dye Alexa 647) cytoplasmic domain of synaptobrevin-2 was tethered to a biotinylated-PEG surface, using 0.1 mg/mL streptavidin and conditions that produced a density of about 200 synaptobrevin-2 molecules per $45 \times 90 \mu\text{m}^2$ field of view. Unbound proteins were subsequently washed away by rinsing three times with 200 μL TBS (20 mM Tris, pH 7.5, 150 mM NaCl). Then, labeled (fluorescent dye Alexa 555) MUN domain was diluted to 100 nM and added in solution with the observation buffer consisting of (1 % (w/v) glucose, 20 mM Tris, pH 7.5, 150 mM NaCl) in the presence of oxygen scavenger (20 units/mL glucose oxidase, 1000 units/mL catalase) and triplet-state quencher (100 μM cyclooctatetraene). Imaging data were collected at a frame rate of 10 Hz for 200 seconds with 635 nm laser light illumination for 5 seconds in order to localize surface-tethered and labeled synaptobrevin-2 molecules. Illumination was then switched to 532 nm laser light and continued for 200 seconds in order to monitor binding events of the labeled MUN domain at the positions of the localized synaptobrevin-2 molecules. A stepwise increase in the fluorescence intensity of the Alexa 555 dye represents a binding event. The gaps between bound states represent unbound periods. Dwell times of the unbound and the bound states were plotted in histograms and fit with single exponential functions to extract the association (k_{on}) and dissociation (k_{off}) rates, respectively.

For the bulk fluorescence anisotropy experiments described in Figures S1D–E, synaptobrevin-2 was labeled with fluorescent dye Alexa 488 at residue 72 and the cytoplasmic domain of syntaxin-1A was labeled with fluorescent dye Alexa 488 at residue 193. Anisotropy was measured with a Synergy 2 microplate reader (BioTek) using an excitation wavelength of 485 ± 20 nm and emission wavelength of 528 ± 20 nm at 26.5°C . The fluorescent dye labeled samples were diluted to 10 nM concentration in TBS (20 mM Tris, pH 7.5, 150 mM NaCl, 0.5 mM TCEP) for optimal read out.

PM and SV vesicles—We used the same membrane compositions and protein densities as in our previous studies (Lai et al., 2016) except that 1 mol% DAG was added to the PM vesicles (except when stated otherwise in Figure S6) and no additional cholesterol was supplemented (see below). The reconstitution method for PM and SV vesicles is described in detail in refs. (Kyoung et al., 2013; Lai et al., 2014). SV vesicles contained both reconstituted synaptotagmin-1 and synaptobrevin-2 (except for the vesicle association experiments shown in Figure S5 which only reconstituted synaptobrevin-2), while PM vesicles contained reconstituted syntaxin-1A and SNAP-25A. For SV vesicles the lipid composition was phosphatidylcholine (PC) (48%), phosphatidylethanolamine (PE) (20%), phosphatidylserine (PS) (12%), and cholesterol (20%). For PM vesicles the lipid composition was Brain Total Lipid Extract (Avanti Polar Lipids) supplemented 3.5 mol% PIP2, 1 mol% DAG, and 0.1 mol% biotinylated phosphatidylethanolamine (PE). For PM vesicles without PIP2 and/or DAG (Figure S6), 1 mol% DAG and/or 3.5 mol% PIP2 was replaced by an equal amount of POPC. Note that Brain Total Lipid Extract contains PS. Quantitative ^{31}P NMR analysis by Avanti Polar Lipids Inc. of two different stocks of Brain Lipid Extract revealed the following average composition of the major components: PC (17%), PE (8%), plasmalogen PE (14%), PS (8%), and sphingomyelin (5%). Among the remaining 48% of other components of Brain Total Lipid Extract is at least 20% cholesterol

(Katyral et al., 1985), so at variance with the previously published protocol (Kyoung et al., 2013) cholesterol was not additionally supplemented to the Brain Total Lipid Extract. Dried lipid films were dissolved in 110 mM OG buffer containing purified proteins at protein-to-lipid ratios of 1:200 for synaptobrevin-2 and syntaxin-1A, and 1:800 for synaptotagmin-1.

A 3–5 fold excess of SNAP-25A (with respect to syntaxin-1A) and 3.5 mol% PIP2 were added to the protein-lipid mixture for PM vesicles only. Detergent-free buffer (20 mM HEPES, pH 7.4, 90 mM NaCl, and 0.1% 2-mercaptoethanol) was added to the protein-lipid mixture until the detergent concentration was at (but not lower than) the critical micelle concentration of 24.4 mM, *i.e.*, vesicle did not yet form. For the preparation of SV vesicles, 50 mM sulforhodamine B (Thermo Fisher Scientific, Inc.) was added to the protein-lipid mixture. The vesicles subsequently formed during size exclusion chromatography using a Sepharose CL-4B column, packed under near constant pressure by gravity with a peristaltic pump (GE Healthcare) in a 5.5 mL column with a ~5 mL bed volume, that was equilibrated with buffer V (20 mM HEPES, pH 7.4, 90 mM NaCl) supplemented with 20 μ M EGTA and 0.1% 2-mercaptoethanol. The eluent was subjected to dialysis into 2 L of detergent-free buffer V supplemented with 20 μ M EGTA, 0.1% 2-mercaptoethanol, 5 g of Bio-beads SM2 and 0.8 g/L Chelex 100 resin. After 4 hours, the buffer was exchanged with 2 L of fresh buffer V supplemented with 20 μ M EGTA, 0.1% 2-mercaptoethanol and Bio-beads, and the dialysis continued for another 12 hours (overnight). We note that for SV vesicles, the chromatography equilibration and elution buffers did not contain sulforhodamine, so the effective sulforhodamine concentration inside SV vesicles is considerably (up to ten-fold) lower than 50 mM.

As described previously (Kyoung et al., 2013), the presence and purity of reconstituted proteins was confirmed by SDS-PAGE of the vesicle preparations (Figure S6), and the directionality of the membrane proteins (facing outward) was assessed by chymotrypsin digestion followed by SDS-PAGE gel electrophoresis. The size distributions of the SV and PM vesicles were frequently analyzed by electron cryo-microscopy, as described previously (Diao et al., 2012).

Single vesicle-vesicle content mixing assay—To monitor SV-PM vesicle association, Ca^{2+} -independent, and Ca^{2+} -triggered fusion we used the single vesicle content mixing assay described in ref. (Lai et al., 2014). The surface of the quartz slides was passivated by coating the surface with polyethylene glycol (PEG) molecules which alleviated non-specific binding of vesicles. The same protocol and quality controls (surface coverage and non-specific binding) were used as described previously (Kyoung et al., 2013) except that PEG-SVA (Laysan Bio) instead of mPEG-SCM (Laysan Bio) was used since it has a longer half-life. The surface was functionalized by inclusion of biotin-PEG (Laysan Bio) during pegylation. A quartz slide was assembled into a flow chamber and incubated with neutravidin for 30 minutes (0.1 mg/mL).

For the fusion experiments described in Figures 2, 3, S2, S6 and S7 biotinylated PM vesicles (100 \times dilution) were pre-incubated with the MUN domain, C1C2BMUN, or C1C2BMUNC2C fragment at the specified concentration for 30 minutes on ice, and then PM vesicles were tethered to the imaging surface by incubation at room temperature (25 $^{\circ}$ C)

for 30 minutes followed by three rounds of washing with 120 μ L buffer V, in order to remove unbound PM vesicles (and the MUN domain in protocol “Pre” in Figure 2); each buffer wash effectively replaces the (3 μ L) flow chamber volume more than 100 times. For the fusion experiments described in Figure 2, the MUN domain was only present during the specified stages. When specified, the C1C2BMUN or C1C2BMUNC2C fragment was present in all stages in Figures 3 and 6, S6, and S7). We found that the pre-incubation of PM vesicles with C1C2BMUN (refers to protocols “All” and “Pre” in Figure 2, and Figures 3, 6, S6, and S7) was important in order to achieve a largest effect on Ca^{2+} -triggered fusion. There was very little change of the distribution of labeled PM vesicles when they were incubated with the C1C2BMUN fragment (at 0.5 μ M) prior to surface-tethering, suggesting that the C1C2BMUN fragment does not cause PM vesicle clustering at that concentration (Figure S4).

For the fusion experiments with complete reconstitution described in Figures 6, S2, biotinylated PM vesicles (100 \times dilution) were tethered to the surface by incubation at room temperature (25 $^{\circ}$ C) for 30 minutes, followed by three rounds of washing with 120 μ L buffer V, in order to remove unbound PM vesicles; each buffer wash effectively replaces the (3 μ L) flow chamber volume more than 100 times. To form syntaxin-1A / Munc18-1 complexes on the PM vesicles, 1 μ M Munc18, 0.5 μ M NSF, 5 μ M α SNAP, 3 mM ATP, 3 mM Mg^{2+} were added and incubated with the surface-tethered PM vesicles at room temperature (25 $^{\circ}$ C) for 30 minutes, followed by three rounds of washing with 120 μ L buffer V. Then the C1C2BMUN fragment (at 0.5 μ M) and 2 μ M SNAP-25A were added and also incubated with the surface-tethered PM vesicles at room temperature (25 $^{\circ}$ C) for 30 minutes, followed by three rounds of washing with 120 μ L buffer V supplemented with 2 μ M SNAP-25A and 0.5 μ M C1C2BMUN fragment. The C1C2MUN fragment and SNAP-25A were present in all stages (Figure 6A). Subsequently, for the fusion experiments shown in Figures 2, 3, 6, S2, S6 and S7, we started the illumination and recording of the fluorescence from a particular field of view of the flow chamber, and loaded SV vesicles (diluted 100 to 1000 times, depending on the acquisition stage, see below) into the flow chamber. Association of SV vesicles with PM vesicles was monitored for 1 minute. The loaded SV vesicle solution was supplemented with 2 μ M complexin-1, along with the MUN domain, C1C2BMUN or C1C2BMUNC2C fragment, and SNAP-25A at the same concentrations as used in the previous stage. While continuing the recording, the flow chamber was washed three times (120 μ L of buffer V supplemented with the same concentrations of complexin-1, MUN, C1C2BMUN, or C1C2BMUNC2C fragment, and SNAP-25A as used in the previous stage) in order to remove unbound SV vesicles. Subsequently, we continued recording for 1 minute to monitor Ca^{2+} -independent fusion events. Thus, in contrast to a previous version of this assay where SV vesicles were incubated with surface-tethered PM vesicles for at least 30 minutes (Kyoung et al., 2013), monitoring of fusion events was started right after the 1 minute SV-PM vesicle association period and buffer washes. Subsequently, Ca^{2+} -solution was injected into the flow chamber consisting of 500 μ M Ca^{2+} , 500 nM Cy5 dye molecules (used as an indicator for the arrival of Ca^{2+} in the evanescent field) in buffer V supplemented with the same concentrations of complexin-1, MUN domain, C1C2BMUN, or C1C2BMUNC2C fragment, and SNAP-25A as used in the previous stage. Ca^{2+} -triggered fusion events were monitored within the same field of view upon injection for a 1 minute

period. The injection was performed at a speed of 66 $\mu\text{L/s}$ by a motorized syringe pump (Harvard Apparatus, Holliston, USA) using a withdrawal method similar to the one described previously (Lai et al., 2014). All experiments were carried out at ambient temperature (25 $^{\circ}\text{C}$). Our procedure resulted in a time series of images over a total of three minutes, consisting of the subsequent 1-min periods of vesicle association, Ca^{2+} -independent, and Ca^{2+} -triggered fusion, plus 5 s intervals for buffer exchanges. The arrival time of Ca^{2+} was determined by monitoring of the Cy5 channel.

For the vesicle association experiments in shown in Figure S5, content-dye labeled, synaptobrevin-2 reconstituted vesicles (diluted 1000 times) were incubated with surface tethered PM-vesicles along with the MUN domain, C1C2BMUN or C1C2BMUNC2C fragment, and labeled vesicles were counted after a 1 minute incubation period.

Data collection and analysis—For the single molecule experiments in Figures 1, 4, 5, S1, and S8 we used an observation buffer consisting of (1 % (w/v) glucose, 20 mM Tris, pH 7.5, 150 mM NaCl) in the presence of oxygen scavenger (20 units/mL glucose oxidase, 1000 units/mL catalase) and triplet-state quencher (100 μM cyclooctatetraene). Imaging data were collected at a frame rate of 10 Hz for 100 seconds until most of the dyes photobleached, with 532 nm laser illumination, using the smCamera program and scripts written for MATLAB (Mathworks). For the smFRET experiments shown in Figures 1, 4, 5 and S8, fluorescence intensity histograms were generated (representative examples are shown in Figures 1D, 1I and 5C) converted to FRET efficiency by

$$E = \frac{I_A - \beta(I_D - \alpha I_A)}{(I_A - \beta(I_D - \alpha I_A)) + (I_D - \alpha I_A)},$$

where αI_A corrects for leakage of acceptor emission into donor channel and βI_D corrects for leakage of donor emission into acceptor channel (McCann et al., 2010). The leakages for our instrument were 16.5% for acceptor fluorescence emission leaking into the donor channel, and 1.7% for donor fluorescence emission leaking into the acceptor channel.

For the experiments described in Figures 1 and 4, the populations of properly assembled subconfigurations (Figures 1F, 1K, 4D, 4H) were calculated as the area under the Gaussian function fit to the high FRET efficiency population divided by the sum of the total efficiency population in the corresponding smFRET histograms in panels E and J, respectively.

For the experiments described in Figure 5, we fit three Gaussian functions to the smFRET histogram of the syntaxin-1A / SNAP-25A complex (green line in Figure 5D) and three Gaussian functions to the smFRET histogram of the syntaxin-1A / Munc18-1 complex (red line in Figure 5D), respectively. The peak position (FRET efficiency = 0.13) of the Gaussian function that fit the low FRET efficiency population in the histogram of the syntaxin-1A / SNAP-25A complex (green line in Figure 5D) was used to define the FRET efficiency of the open state of syntaxin-1A. The peak position (FRET efficiency = 0.71) of the Gaussian function that fit the high FRET efficiency population in the histogram of the syntaxin-1A / Munc18-1 complex (red line in Figure 5D) was used to define the FRET efficiency of the

closed state of syntaxin-1A. The FRET efficiencies of the open and closed states were then used as constraints for fitting three Gaussian functions to the FRET efficiency histograms shown in Figure 5. The quantity “% closed state” was calculated as the area under the Gaussian function fit to the population of the closed state divided by the total area under the fitted three Gaussian functions (Figure 5G, Table S5).

For the fusion experiments described in Figures 2, 3, 6, S2, and S6, S7, in order to increase the throughput of the assay and make better use of the vesicle samples, after intensive washing ($3 \times 120 \mu\text{L}$) with buffer V (supplemented with $20 \mu\text{M}$ EGTA to remove Ca^{2+} from the sample chamber), we repeated the entire acquisition sequence (SV vesicle loading, counting the number of freshly associated SV-PM vesicles, monitoring of Ca^{2+} -independent fusion, Ca^{2+} -injection, and monitoring of Ca^{2+} -triggered fusion) in a different imaging area within the same flow chamber. Five such *acquisition rounds* were performed with the same sample chamber. SV vesicles were diluted $1000\times$ for the first and second acquisition rounds, $200\times$ for the third and fourth acquisition rounds, and $100\times$ for the fifth acquisition round in order to offset the slightly increasing saturation of the surface with SV vesicles. The entire experiment (each with five acquisition rounds) was then repeated n times (Tables S3–S4, and S7) (referred to as *repeat experiment*). Among the specified number of repeats there are at least three different protein preparations and vesicle reconstitutions, so the variations observed in the bar charts reflect sample variations as well as variations among different flow chambers.

We detected content dye fluorescent spots in a particular imaging area with the smCamera program. The appearance of a content dye fluorescence spot corresponds to an association of a SV vesicle to a surface-tethered PM vesicle. However, only those spots were subsequently analyzed and counted that showed *exactly one* stepwise increase of the fluorescence intensity during the SV-PM vesicle association period of 1 minute that precedes the subsequent fusion periods (Figures 2A, 3A and 6A). Thus, this procedure excludes SV vesicles that underwent Ca^{2+} -independent fusion during the vesicle association period since fusion leads to a second stepwise fluorescence intensity increase. Moreover, for data acquisition rounds within the same sample chamber, this procedure excludes SV vesicles that were already associated during a previous acquisition round. Stepwise increases in the fluorescence intensity time traces were automatically detected by the computer program described in ref. (Kyoung et al., 2013) and manually checked to ensure correct performance of the automated procedure. Collectively, we refer this selected set of content dye fluorescent spots as the analyzed SV-PM vesicle pairs.

In the subsequent Ca^{2+} -independent and Ca^{2+} -triggered fusion periods of 1 minute each, a second stepwise increase in content dye fluorescence intensity was counted as a Ca^{2+} -independent and Ca^{2+} -triggered fusion event, respectively. Histograms for Ca^{2+} -independent and Ca^{2+} -triggered fusion events were generated with a time bin of 1 second. Ca^{2+} -triggered fusion histograms were synchronized by the appearance of fluorescence intensity of the Cy5 dye molecules that are part of the injected Ca^{2+} -solution. Histograms were cumulated over all acquisition rounds and repeat experiments. The cumulated histograms were subsequently *normalized* by dividing the histograms by the total number of analyzed SV-PM vesicle pairs for a particular condition (i.e., the sum of the number of analyzed SV-PM vesicle pairs for

all acquisition rounds and repeat experiments for a particular condition) (Tables S3–S4, and S7, Figure S2). As a consequence of the normalization of the histograms, the fusion probabilities and amplitudes are normalized with respect to the corresponding number of analyzed SV-PM vesicle pairs. Thus, the normalized fusion probabilities and amplitudes provide information about fusion of associated SV-PM vesicles, independent of the number of associated vesicle pairs. This is a major advantage of our single vesicle method over bulk fusion assays which cannot distinguish between effects that are due to vesicle association or fusion itself (Brunger et al., 2015).

In the bar charts in Figures 2, 3, 6, S6 and S7, the probability of Ca^{2+} -independent fusion per second is calculated by dividing the overall Ca^{2+} -independent fusion probability of the cumulated and normalized histogram during the 1-minute observation period by 60. The “ Ca^{2+} -triggered amplitude” is the probability of Ca^{2+} -triggered fusion in the cumulated and normalized histogram during the first time bin (1 second) upon Ca^{2+} -injection. The “fusion ratio” is the ratio of the Ca^{2+} -triggered amplitude and the average probability of Ca^{2+} -independent fusion per second. The error bars for the probabilities and amplitudes were calculated as standard deviations for the n repeat experiments (Tables S3–S4 and S7) by using individually-cumulated (but globally normalized) histograms for all rounds of a particular repeat experiment. The histograms of the Ca^{2+} -triggered fusion probability (Figure S2) were fit to a single exponential decay function using the Levenberg-Marquardt algorithm. The degree of synchronization was described by the decay rate and error bars for the decay rate were obtained from the covariance matrix of the fit.

MUN domain removal experiment—For the experiments shown in Figure S3, we used the protocol “Pre” shown in Figure 2A, except that 500 nM of labeled MUN domain was mixed with 9.5 μM unlabeled MUN domain. Labeling of the MUN domain was performed with the Alexa 647 fluorescent dye by covalently linking it to the primary amino group. The percentage of MUN domain molecules that are bound to SV vesicles was calculated by co-localizing the spots in “red” channel that detects the fluorescence intensity of Alexa 647 labeled MUN domain molecules and the spots in the “green” channel that detects the fluorescence intensity of content dye labeled SV vesicles. The co-localization was measured before and after MUN domain molecules were washed away by rinsing with buffer V.

Neuronal cultures—For the experiments described in Figure 7, micro-island cultures of hippocampal neurons were prepared and cultured as previously reported (Jockusch et al., 2007; Burgalossi et al., 2012). Briefly, astrocytes for autaptic cultures were obtained from mouse cortices dissected from P0 wild type animals and enzymatically digested for 15 min at 37 °C with 0.25% (w/v) trypsin-EDTA (Gibco). Astrocytes were plated in T75 culture flasks in DMEM medium (Gibco) containing 10% FBS and penicillin (100 U/mL)/streptomycin (100 $\mu\text{g/mL}$), and grown for 7–10 days *in vitro* (DIV). After this, astrocytes were trypsinized and plated at a density of ~30,000 cells/well onto 32 mm-diameter glass coverslips that were previously coated with agarose (Sigma-Aldrich), and stamped using a custom-made stamp to generate 200 $\mu\text{m} \times 200 \mu\text{m}$ substrate islands with a coating solution containing poly-D-lysine (Sigma-Aldrich), acetic acid, and collagen (BD Biosciences). Hippocampi from Munc13-1/2 double-knockout embryo 18 (E18) mice were isolated and

digested for 55 min at 37 °C in DMEM medium containing 2.5 U/mL papain (Worthington Biomedical Corporation), 0.2 mg/mL cysteine (Sigma), 1 mM CaCl₂, and 0.5 mM EDTA. After washing, the dissociated neurons were seeded onto the micro-island plates in pre-warmed Neurobasal medium (Gibco) supplemented with B27 (Gibco), Glutamax (Gibco) and penicillin (100 U/mL)/streptomycin (100 µg/mL) at a density of ~4,000 cell/well. Neurons were allowed to mature for 10–28 days before they were used for experiments, and only islands containing single neurons were examined.

Experiments with Semliki Forest virus—For the experiments described in Figure 7, generation of Semliki Forest virus constructs with Munc13-1-EGFP, or syntaxin-1A^{LE}-IRES-GFP, generation of virus stocks and neuron infection were performed as previously described (Ashery et al., 1999). To activate the frozen viruses (450 µL) including either Munc13-1 or syntaxin-1A^{LE} genes, 450 mL neuronal medium from the neuronal culture was added. 100 µL chymotrypsin (2 mg/mL, Boehringer Mannheim) was added and incubated for 50–55 minutes at room temperature. In order to inactivate the activity of chymotrypsin, the virus was incubated with 110 µL aprotinin (6 mg/mL, Boehringer Mannheim) for 15 minutes. Infection of neurons was performed by adding 30 µL of the activated viruses into autaptic Munc13-1/2 double-knockout neuronal cultures, which were placed in the incubator for 12 hours.

Western blotting—For the experiments described in Figure 7, hippocampal neurons prepared from Munc13-1/2 double-knockout embryo 18 (E18) mice were infected with activated Semliki Forest virus expressing GFP, Munc13-1 or syntaxin-1A^{LE}. The lysates were harvested after 12 h for Munc13-1 or 18 h for syntaxin-1A^{LE} expressing neurons and analyzed by Western blotting using anti-Munc13-1 rabbit antibody (SySy, Cat#126 103) or anti-syntaxin-1 mouse antibody (SySy, Cat#110 011). Mouse anti-tubulin (Sigma, Cat#T4026) or rabbit anti-actin (Sigma-A5060) antibody were used as loading controls for Munc13-1 and syntaxin-1A, respectively. For quantitation, goat anti-rabbit IgG-IRDye800 (Rockland, Cat#611-132-122) and goat anti-mouse IgG-IRDye700 (Rockland, Cat#610-130-121) secondary antibodies were used, and imaged on an Odyssey Infrared Imaging System (LI-COR Biosciences). For quantification of syntaxin-1A^{LE} overexpression, the fluorescence signal from the syntaxin-1 band was normalized by the signal from the actin band. For quantification of Munc13-1 overexpression, the fluorescence signal from the Munc13-1 band was normalized by the signal from the tubulin band. Relative syntaxin-1 protein amounts were calculated by normalization to GFP expressing neurons.

Electrophysiology—For electrophysiology experiments described in Figure 7, autaptic cultured neurons (12–14 DIV) were whole-cell voltage-clamped at –70 mV with an Axopatch 700B (Molecular Devices). All traces were analyzed using AxoGraph X (AxoGraph Scientific). Series resistance was within 10 MΩ and was electronically compensated at least 30–70%. The experiments were performed using a patch-pipette solution containing 136 mM KCl, 17.8 mM, 1 mM EGTA, 0.6 mM, 4 mM NaATP, 0.3 mM Na₂GTP, 15 creatine phosphate, and 5 U/mL phosphocreatine kinase (315–320 mOsmol/L, pH 7.4). The extracellular solution used for all recordings contained 140 mM NaCl, 2.4 mM

KCl, 10 mM Hepes, 10 mM glucose, 4 mM CaCl₂ and 4 mM MgCl₂ (320 mOsm/L), pH, 7.3. Evoked EPSCs were induced by depolarizing the cell from -70 to 0 mV at a frequency of 0.2 Hz. Only a subset of the Munc13 KDO neurons that were infected with the syntaxin-1A^{LE} construct exhibited action-driven potentials, and even fewer exhibited spontaneous release within a 100 sec time period. Only those that showed responses were included in the analyses shown in Figures 7D–N. The size of the readily releasable pool (RRP) was measured after 6 s application of 0.5 M hypertonic sucrose solution. Short-term plasticity was evaluated by recording EPSCs during 10 Hz stimulation trains. All electrophysiological traces were analyzed using Axograph X software (version 1.4.3, AxoGraph Scientific).

Quantification and Statistical Analysis

Origin, Matlab, and Igor was used for the generation of all curves and graphs. The fusion experiments described in Figures 2, 3, 6, S2, S6, S7 were conducted at least three times with different protein preparations and vesicle reconstitutions and properties were calculated as mean \pm SD, for n experimental repeats (specified in Tables S3–S6 and S9) and the statistical significance was assessed using Student's t-test with respect to the specified reference experiment. For the smFRET efficiency properties shown in Figures 1F, 1K, 4D, 4H, 5G, S8E mean values \pm SD were calculated for $n=2$ subsets of an equal partition of the data. For the single molecule incorporation data in Figures 1C, 1H, 4B, 4F, S8B mean values \pm SD were calculated from $n=3$ independent fields of view. All results in Figure 7 are shown as mean values \pm SEM, using the specified number of neurons and mice as specified in the figure and figure legend. Statistical significance was assessed using one-way ANOVA followed by post-hoc Bonferroni test or by two-tailed Student's t-test, where appropriate. For all the statistical test, the significance is defined as: * $p < 0.05$ ** $p < 0.01$ and *** $p < 0.001$. No method was used to determine if the data meet assumptions of the statistical approach.

KEY RESOURCES TABLE

REAGENT or RESOURCE	SOURCE	IDENTIFIER
Antibodies		
Rabbit anti-Actin	Sigma	Cat#A5060; RRID: AB_476738
Mouse anti-Syntaxin-1	SySy	Cat#110 011; RRID: AB_887842
Rabbit anti-Munc13-1	SySy	Cat#126 103; RRID: AB_887733
Mouse anti-Tubulin	Sigma	Cat#T4026; RRID: AB_477577
Goat anti-Rabbit IgG-IRDye800	Rockland	Cat#611-132-122; RRID: AB_220152
Goat anti-Mouse IgG-IRDye700	Rockland	Cat#610-130-121; RRID: AB_220121
Bacterial and Virus Strains		
Biological Samples		

REAGENT or RESOURCE	SOURCE	IDENTIFIER
Chemicals, Peptides, and Recombinant Proteins		
Alexa 488 C5	Thermo Fisher Scientific Inc.	Cat#A10254
Alexa 555 C2	Thermo Fisher Scientific Inc.	Cat#A20346
Alexa 647 C2	Thermo Fisher Scientific Inc.	Cat#A20347
Alexa 555 NHS Ester	Thermo Fisher Scientific Inc.	Cat#A20009
glucose oxidase	Sigma	Cat#G2133
catalase	Sigma	Cat#C100
glucose	Sigma	Cat#D9434
cyclooctatetraene	Sigma	Cat#138924
egg phosphatidylcholine (PC)	Avanti Polar Lipid	Cat#840051
Brain total lipid extract		Cat#131101C
1-Palmitoyl-2-oleoyl-sn-glycero-3-phosphocholine (POPC)	Avanti Polar Lipid	Cat#850457C
1,2-Dioleoyl-sn-glycerol-3-phosphoethanolamine (DOPE)	Avanti Polar Lipid	Cat#850725C
1,2-dioleoyl-sn-glycero-3-phospho-L-serine (DOPS)	Avanti Polar Lipid	Cat#840035C
Cholesterol	Avanti Polar Lipid	Cat#70000P
L- α -phosphatidylinositol-4,5-bisphosphate (PIP2)	Avanti Polar Lipid	Cat#8400046X
1-2-dioleoyl-sn-glycerol	Avanti Polar Lipid	Cat#800811
1-Oleoyl-2-(12-biotinyl(aminododecanoyl))-sn-glycero-3-phosphoethanolamine (Biotin-PE)	Avanti Polar Lipid	Cat#860562C
sulforhodamine B	Invitrogen	Cat#S1307
mPEG-SVA	Laysan Bio	Cat#mPEG-SVA-5000
Biotin-PEG-SVA-5000	Laysan Bio	Cat#Biotin-PEG-SVA-5000
DMEM medium	Gibco	Cat#41966-029
Neurobasal A medium	Gibco	Cat#10888-022
NBQX disodium salt	Tocris Bioscience	Cat#1044
Tetrodotoxin (TTX)	Tocris Bioscience	Cat#1078
(-)-Bicuculline methochloride	Tocris Bioscience	Cat#0131
Calcium Ionophore A23187	HelloBio	Cat#HB1000
Critical Commercial Assays		
Deposited Data		
Experimental Models: Cell Lines		
Sf9 insect cell	Gibco	Cat#11496015
E.Coli.DH10 Bac	Thermo Fisher Scientific	Cat#10361012
E.coli. BL21 (DE3)	Invitrogen	Cat#C600003
Experimental Models: Organisms/Strains		

REAGENT or RESOURCE	SOURCE	IDENTIFIER
Mouse: M13-DKO: Unc13atm1Bros; Unc13btm1Rmnd	(Augustin et al., 1999; Varoqueaux et al., 2002)	RRID: MGI2654056
Oligonucleotides		
Recombinant DNA		
pACYC184-BirA	Avidity	Cat#AVB101
Munc13-1-EGFP	(Ashery et al., 1999)	N/A
syntaxin-1ALE-IRES-GFP	(Richmond et al., 2001)	N/A
Software and Algorithms		
OriginPro	Origin lab	http://www.originlab.com/
Matlab	MathWorks	https://www.mathworks.com/
Igor	WaveMetrics	https://www.wavemetrics.com/products/igorpro/igorpro.htm
smCamera	Taekjip Ha	http://ha.med.jhmi.edu/resources/#1464200861600-0fad9996-bfd4
GraphPad Prism 5	GraphPad Software, Inc	http://www.graphpad.com/
AxoGraph Version 1.4.3	John Clements	https://www.axograph.com/
Other		

Supplementary Material

Refer to Web version on PubMed Central for supplementary material.

Acknowledgments

We thank J. Diao, P. Gipson, C. Ma, T.C. Südhof, W.I. Weis, and K.I. White for discussions, L. Almagor for help with fluorescence anisotropy experiments, J. Rizo for providing expression constructs, T. Ha for the smCamera program, Y. Zhang for a fusion analysis program, and the National Institutes of Health for support (R37-MH63105 to ATB).

References

- Aravamudan B, Fergestad T, Davis WS, Rodesch CK, Broadie K. Drosophila UNC-13 is essential for synaptic transmission. *Nat Neurosci.* 1999; 2:965–971. [PubMed: 10526334]
- Ashery U, Betz A, Xu T, Brose N, Rettig J. An efficient method for infection of adrenal chromaffin cells using the Semliki Forest virus gene expression system. *Eur J Cell Biol.* 1999; 78:525–532. [PubMed: 10494858]
- Augustin I, Rosenmund C, Südhof TC, Brose N. Munc13-1 is essential for fusion competence of glutamatergic synaptic vesicles. *Nature.* 1999; 400:457–461. [PubMed: 10440375]
- Baker RW, Jeffrey PD, Zick M, Phillips BP, Wickner WT, Hughson FM. A direct role for the Sec1/Munc18-family protein Vps33 as a template for SNARE assembly. *Science* (80–). 2015; 349:1111–1114.

- Basu J, Shen N, Dulubova I, Lu J, Guan R, Guryev O, Grishin NV, Rosenmund C, Rizo J. A minimal domain responsible for Munc13 activity. *Nat Struct Mol Biol.* 2005; 12:1017–1018. [PubMed: 16228007]
- Boswell KL, James DJ, Esquibel JM, Bruinsma S, Shirakawa R, Horiuchi H, Martin TFJ. Munc13-4 reconstitutes calcium-dependent SNARE-mediated membrane fusion. *J Cell Biol.* 2012; 197:301–312. [PubMed: 22508512]
- Breustedt J, Gundlfinger A, Varoqueaux F, Reim K, Brose N, Schmitz D. Munc13-2 differentially affects hippocampal synaptic transmission and plasticity. *Cereb Cortex.* 2010; 20:1109–1120. [PubMed: 19700493]
- Brunger AT. Structure and function of SNARE and SNARE-interacting proteins. *Q Rev Biophys.* 2006; 38:1.
- Brunger AT, Cipriano DJ, Diao J. Towards reconstitution of membrane fusion mediated by SNAREs and other synaptic proteins. *Crit Rev Biochem Mol Biol.* 2015; 0:1–11.
- Burgalossi A, Jung S, Man KM, Nair R, Jockusch WJ, Wojcik SM, Brose N, Rhee JS. Analysis of neurotransmitter release mechanisms by photolysis of caged Ca²⁺ in an autaptic neuron culture system. *Nat Protoc.* 2012; 7:1351–1365. [PubMed: 22722370]
- Chen X, Lu J, Dulubova I, Rizo J. NMR analysis of the closed conformation of syntaxin-1. *J Biomol NMR.* 2008; 41:43–54. [PubMed: 18458823]
- Chen YA, Scales SJ, Scheller RH. Sequential SNARE assembly underlies priming and triggering of exocytosis. *Neuron.* 2001; 30:161–170. [PubMed: 11343652]
- Choi UB., Weninger, KR., Bowen, ME. *Intrinsically Disordered Protein Analysis.* New York, NY: Springer New York; 2012. *Immobilization of Proteins for Single-Molecule Fluorescence Resonance Energy Transfer Measurements of Conformation and Dynamics*; p. 3-20.
- Choi UB, Zhao M, Zhang Y, Lai Y, Brunger AT. Complexin induces a conformational change at the membrane-proximal C-terminal end of the SNARE complex. *Elife.* 2016; 5:e16886. [PubMed: 27253060]
- Diao J, Grob P, Cipriano DJ, Kyoung M, Zhang Y, Shah S, Nguyen A, Padolina M, Srivastava A, Vrljic M, et al. Synaptic proteins promote calcium-triggered fast transition from point contact to full fusion. *Elife.* 2012; 1:e00109. [PubMed: 23240085]
- Dulubova I, Sugita S, Hill S, Hosaka M, Fernandez I, Südhof TC, Rizo J. A conformational switch in syntaxin during exocytosis: role of munc18. *EMBO J.* 1999; 18:4372–4382. [PubMed: 10449403]
- Fasshauer D, Margittai M. A transient N-terminal interaction of SNAP-25 and syntaxin nucleates SNARE assembly. *J Biol Chem.* 2004; 279:7613–7621. [PubMed: 14665625]
- Fernández-Chacón R, Königstorfer A, Gerber SHH, García J, Matos MFF, Stevens CFF, Brose N, Rizo J, Rosenmund C, Südhof TCC. Synaptotagmin I functions as a calcium regulator of release probability. *Nature.* 2001; 410:41–49. [PubMed: 11242035]
- Geppert M, Goda Y, Hammer RERERE, Li C, Rosahl TWTWTW, Stevens CFCFCF, Südhof TCTCTC, Augustine GJ, Eckert R, Barrett EF, et al. Synaptotagmin I: A major Ca²⁺ sensor for transmitter release at a central synapse. *Cell.* 1994; 79:717–727. [PubMed: 7954835]
- Gipson P, Fukuda Y, Danev R, Lai Y, Chen D-H, Baumeister W, Brunger AT. Morphologies of synaptic protein membrane fusion interfaces. *Proc Natl Acad Sci U S A.* 2017 in press.
- Guan R, Dai H, Rizo J. Binding of the Munc13-1 MUN domain to membrane-anchored SNARE complexes. *Biochemistry.* 2008; 47:1474–1481. [PubMed: 18201107]
- Hammarlund M, Palfreyman MT, Watanabe S, Olsen S, Jorgensen EM. Open syntaxin docks synaptic vesicles. *PLoS Biol.* 2007; 5:e198. [PubMed: 17645391]
- Heidelberger R, Heinemann C, Neher E, Matthews G. Calcium dependence of the rate of exocytosis in a synaptic terminal. *Nature.* 1994; 371:513–515. [PubMed: 7935764]
- Imig C, Min SW, Krinner S, Arancillo M, Rosenmund C, Südhof TC, Rhee J, Brose N, Cooper BH. The Morphological and Molecular Nature of Synaptic Vesicle Priming at Presynaptic Active Zones. *Neuron.* 2014; 84:416–431. [PubMed: 25374362]
- Jockusch WJ, Speidel D, Sigler A, Sørensen JB, Varoqueaux F, Rhee JS, Brose N. CAPS-1 and CAPS-2 are essential synaptic vesicle priming proteins. *Cell.* 2007; 131:796–808. [PubMed: 18022372]

- Junge HJ, Rhee J, Jahn O, Varoqueaux F, Spiess J, Waxham MN, Rosenmund C, Brose N. Calmodulin and Munc13 Form a Ca²⁺ Sensor/Effector Complex that Controls Short-Term Synaptic Plasticity. *Cell*. 2004; 118:389–401. [PubMed: 15294163]
- Katyal SL, Barilaro L, Hanin I. Lipid composition of different areas of murine brain: effects of lipid extraction procedures. *Lipids*. 1985; 20:201–203. [PubMed: 3990528]
- Koch H, Hofmann K, Brose N. Definition of Munc13-homology-domains and characterization of a novel ubiquitously expressed Munc13 isoform. *Biochem J*. 2000; 349:247–253. [PubMed: 10861235]
- Kyoung M, Zhang Y, Diao J, Chu S, Brunger AT. Studying calcium-triggered vesicle fusion in a single vesicle-vesicle content and lipid-mixing system. *Nat Protoc*. 2013; 8:1–16. [PubMed: 23222454]
- Lai Y, Diao J, Cipriano DJ, Zhang Y, Pfuetzner Ra, Padolina MS, Brunger AT. Complexin inhibits spontaneous release and synchronizes Ca²⁺-triggered synaptic vesicle fusion by distinct mechanisms. *Elife*. 2014; 3:e03756. [PubMed: 25122624]
- Lai Y, Choi UB, Zhang Y, Zhao M, Pfuetzner RA, Wang AL, Diao J, Brunger AT. N-terminal domain of complexin independently activates calcium-triggered fusion. *Proc Natl Acad Sci*. 2016; 113:E4698–E4707. [PubMed: 27444020]
- Lipstein N, Schaks S, Dimova K, Kalkhof S, Ihling C, Kolbel K, Ashery U, Rhee J, Brose N, Sinz a, et al. Nonconserved Ca²⁺/Calmodulin Binding Sites in Munc13s Differentially Control Synaptic Short-Term Plasticity. *Mol Cell Biol*. 2012; 32:4628–4641. [PubMed: 22966208]
- Liu X, Seven AB, Camacho M, Esser V, Xu J, Trimbuch T, Quade B, Su L, Ma C, Rosenmund C, et al. Functional synergy between the Munc13 C-terminal C1 and C2 domains. *Elife*. 2016; 5:1–27.
- Ma C, Li W, Xu Y, Rizo J. Munc13 mediates the transition from the closed syntaxin-Munc18 complex to the SNARE complex. *Nat Struct Mol Biol*. 2011; 18:542–549. [PubMed: 21499244]
- Ma C, Su L, Seven AB, Xu Y, Rizo J. Reconstitution of the vital functions of Munc18 and Munc13 in neurotransmitter release. *Science*. 2013; 339:421–425. [PubMed: 23258414]
- McCann JJ, Choi UB, Zheng L, Weninger K, Bowen ME. Optimizing methods to recover absolute FRET efficiency from immobilized single molecules. *Biophys J*. 2010; 99:961–970. [PubMed: 20682275]
- McMahon HT, Missler M, Li C, Südhof TC. Complexins: Cytosolic proteins that regulate SNAP receptor function. *Cell*. 1995; 83:111–119. [PubMed: 7553862]
- Misura KM, Scheller RH, Weis WI. Three-dimensional structure of the neuronal-Sec1-syntaxin 1a complex. *Nature*. 2000; 404:355–362. [PubMed: 10746715]
- Mohrmann R, Dhara M, Bruns D. Complexins: small but capable. *Cell Mol Life Sci*. 2015
- Pevsner J, Hsu SC, Braun JE, Calakos N, Ting aE, Bennett MK, Scheller RH. Specificity and regulation of a synaptic vesicle docking complex. *Neuron*. 1994; 13:353–361. [PubMed: 8060616]
- Rhee JS, Betz A, Pyott S, Reim K, Varoqueaux F, Augustin I, Hesse D, Südhof TC, Takahashi M, Rosenmund C, et al. Beta phorbol ester- and diacylglycerol-induced augmentation of transmitter release is mediated by Munc13s and not by PKCs. *Cell*. 2002; 108:121–133. [PubMed: 11792326]
- Richmond JE, Davis WS, Jorgensen EM. UNC-13 is required for synaptic vesicle fusion in *C. elegans*. *Nat Neurosci*. 1999; 2:959–964. [PubMed: 10526333]
- Richmond JE, Weimer RM, Jorgensen EM. An open form of syntaxin bypasses the requirement for UNC-13 in vesicle priming. *Nature*. 2001; 412:338–341. [PubMed: 11460165]
- Rickman C, Davletov B. Arachidonic Acid Allows SNARE Complex Formation in the Presence of Munc18. *Chem Biol*. 2005
- Rosenmund C, Sigler A, Augustin I, Reim K, Brose N, Rhee JS. Differential Control of Vesicle Priming and Short-Term Plasticity by Munc13 Isoforms. *Neuron*. 2002; 33:411–424. [PubMed: 11832228]
- Rothman JE. The Principle of Membrane Fusion in the Cell (Nobel Lecture). *Angew Chemie Int Ed*. 2014 n/a–n/a.
- Schneggenburger R, Neher E. Intracellular calcium dependence of transmitter release rates at a fast central synapse. *Nature*. 2000; 406:889–893. [PubMed: 10972290]

- Shin OH, Lu J, Rhee JS, Tomchick DR, Pang ZP, Wojcik SM, Camacho-Perez M, Brose N, Machius M, Rizo J, et al. Munc13 C2B domain is an activity-dependent Ca²⁺ regulator of synaptic exocytosis. *Nat Struct Mol Biol.* 2010; 17:280–288. [PubMed: 20154707]
- Stevens DR, Wu ZX, Matti U, Junge HJ, Schirra C, Becherer U, Wojcik SM, Brose N, Rettig J. Identification of the minimal protein domain required for priming activity of munc13-1. *Curr Biol.* 2005; 15:2243–2248. [PubMed: 16271475]
- Südhof TC. The presynaptic active zone. *Neuron.* 2012; 75:11–25. [PubMed: 22794257]
- Südhof TCC. Neurotransmitter release: the last millisecond in the life of a synaptic vesicle. *Neuron.* 2013; 80:675–690. [PubMed: 24183019]
- Sutton RB, Fasshauer D, Jahn R, Brunger AT. Crystal structure of a SNARE complex involved in synaptic exocytosis at 2.4 Å resolution. *Nature.* 1998; 395:347–353. [PubMed: 9759724]
- Trimbuch T, Rosenmund C. Should I stop or should I go? The role of complexin in neurotransmitter release. *Nat Rev Neurosci.* 2016; 17:118–125. [PubMed: 26806630]
- Varoqueaux F, Sigler A, Rhee JS, Brose N, Enk C, Reim K, Rosenmund C. Total arrest of spontaneous and evoked synaptic transmission but normal synaptogenesis in the absence of Munc13-mediated vesicle priming. *Proc Natl Acad Sci U S A.* 2002; 99:9037–9042. [PubMed: 12070347]
- Verhage M, Maia AS, Plomp JJ, Brussaard AB, Heeroma JH, Vermeer H, Toonen RF, Hammer RE, van den Berg TK, Missler M, et al. Synaptic assembly of the brain in the absence of neurotransmitter secretion. *Sci (New York, NY).* 2000; 287:864–869.
- Wang S, Choi UB, Gong J, Yang X, Li Y, Wang AL, Yang X, Brunger AT, Ma C. Conformational change of syntaxin linker region induced by Munc13s initiates SNARE complex formation in synaptic exocytosis. *EMBO J.* 2017; 36:816–829. [PubMed: 28137749]
- Wang SSH, Held RG, Wong MY, Liu C, Karakhanyan A, Kaeser PS. Fusion Competent Synaptic Vesicles Persist upon Active Zone Disruption and Loss of Vesicle Docking. *Neuron.* 2016; 91:777–791. [PubMed: 27537483]
- Weber T, Zemelman BV, McNew JA, Westermann B, Gmachl M, Parlati F, Söllner TH, Rothman JE. SNAREpins: minimal machinery for membrane fusion. *Cell.* 1998; 92:759–772. [PubMed: 9529252]
- Weninger K, Bowen ME, Chu S, Brunger AT. Single-molecule studies of SNARE complex assembly reveal parallel and antiparallel configurations. *Proc Natl Acad Sci U S A.* 2003; 100:14800–14805. [PubMed: 14657376]
- Weninger K, Bowen ME, Choi UB, Chu S, Brunger AT. Accessory proteins stabilize the acceptor complex for synaptobrevin, the 1:1 syntaxin/SNAP-25 complex. *Structure.* 2008; 16:308–320. [PubMed: 18275821]
- Winter U, Chen X, Fasshauer D. A conserved membrane attachment site in alpha-SNAP facilitates N-ethylmaleimide-sensitive factor (NSF)-driven SNARE complex disassembly. *J Biol Chem.* 2009; 284:31817–31826. [PubMed: 19762473]
- Woodbury D. The t-SNARE syntaxin is sufficient for spontaneous fusion of synaptic vesicles to planar membranes. *Cell Biol Int.* 2000; 24:809–818. [PubMed: 11067766]
- Xu J, Pang ZP, Shin OH, Südhof TC. Synaptotagmin-I functions as a Ca²⁺ sensor for spontaneous release. *Nat Publ Gr.* 2009; 12:759–766.
- Xu J, Camacho M, Xu Y, Esser V, Liu X, Trimbuch T, Pan Y-Z, Ma C, Tomchick DR, Rosenmund C, et al. Mechanistic insights into neurotransmitter release and presynaptic plasticity from the crystal structure of Munc13-1 C1C2 BMUN. *Elife.* 2017:6.
- Yang B, Steegmaier M, Gonzalez LC, Scheller RH. nSec1 binds a closed conformation of syntaxin1A. *J Cell Biol.* 2000; 148:247–252. [PubMed: 10648557]
- Yang X, Wang S, Sheng Y, Zhang M, Zou W, Wu L, Kang L, Rizo J, Zhang R, Xu T, et al. Syntaxin opening by the MUN domain underlies the function of Munc13 in synaptic-vesicle priming. *Nat Struct Mol Biol.* 2015; 22:547–554. [PubMed: 26030875]
- Zhou Q, Lai Y, Bacaj T, Zhao M, Lyubimov AY, Uervirojnangkoorn M, Zeldin OB, Brewster AS, Sauter NK, Cohen AE, et al. Architecture of the synaptotagmin–SNARE machinery for neuronal exocytosis. *Nature.* 2015; 525:62–67. [PubMed: 26280336]
- Zhou Q, Zhou P, Wang AL, Wu D, Zhao M, Südhof TC, Brunger AT. The primed SNARE-complexin-synaptotagmin complex for neuronal exocytosis. *Nature.* 2017 in press.

Zick M, Wickner WT. A distinct tethering step is vital for vacuole membrane fusion. *Elife*. 2014; 3:e03251. [PubMed: 25255215]

Author Manuscript

Author Manuscript

Author Manuscript

Author Manuscript

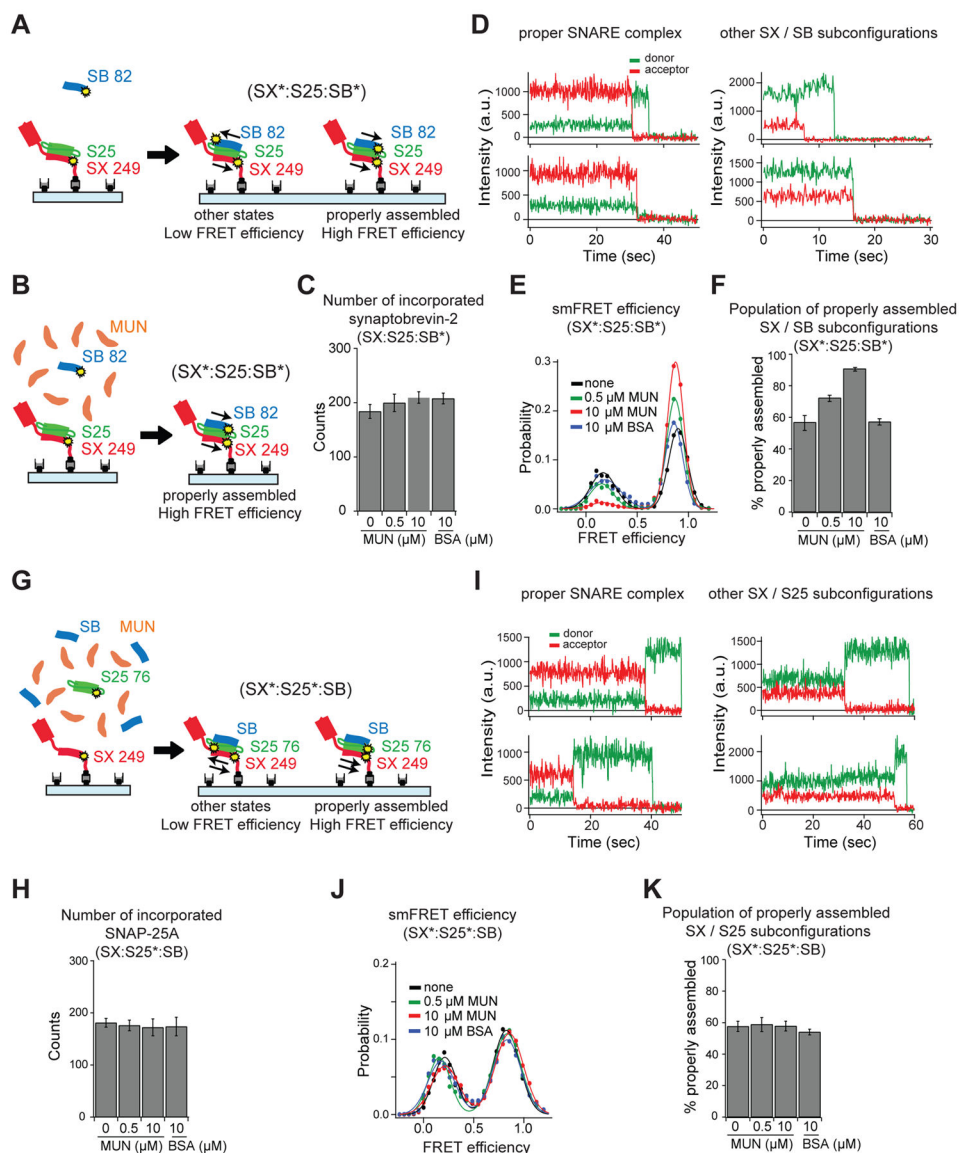


Figure 1. The MUN domain alone promotes the proper syntaxin-1A / synaptobrevin-2 subconfiguration, but not the syntaxin-1A / SNAP-25A subconfiguration
 (A, B, G) The syntaxin-1A (SX) / synaptobrevin-2 (SB) and the syntaxin-1A / SNAP-25A (S25) subconfigurations of the ternary SNARE complex were probed by single molecule experiments. The yellow dots and the asterisks (*) indicate fluorescently labeled residues. The cytoplasmic domain of SX was tethered on a PEG-passivated microscope slide via streptavidin-biotin linkage and labeled with Alexa 647 at residue 249. The cytoplasmic domain of SB was labeled with Alexa 555 at residue 82 and S25 was labeled with Alexa 555 at residue 76. The thin arrows represent parallel or antiparallel SX / SB (A, B) or SX / S25 (G) subconfigurations. (A, B) Beginning with surface-tethered SX, the binary complex with S25 was first formed, and then SB, was added in the absence (A) or in the presence (B) of the MUN domain at the specified concentration or BSA control. (G) Beginning with surface-tethered SX, the ternary SNARE complex was formed by adding S25 and SB at the same

time in the presence of the MUN domain at the specified concentration or BSA control. (C, H) Mean counts from three fields of view \pm SD (Table S1) of SB (C) or S25 (H) incorporation into the ternary SNARE complex in presence of the MUN domain at the specified concentrations or BSA control. (D, I) Representative fluorescence intensity time traces of properly (left panels) and improperly (right panels) assembled SNARE complexes that were formed starting from surface-tethered SX / S25 complex (D) or from surface-tethered SX molecules (I) in the absence of the MUN domain. (E, J) smFRET efficiency histograms using labeled SB (E), or S25 (J). (F, K) Percent of properly assembled SX / SB (F), or SX / S25 (K) subconfigurations. Shown are means \pm SD for the two subsets of an equal partition of the data (Table S2).

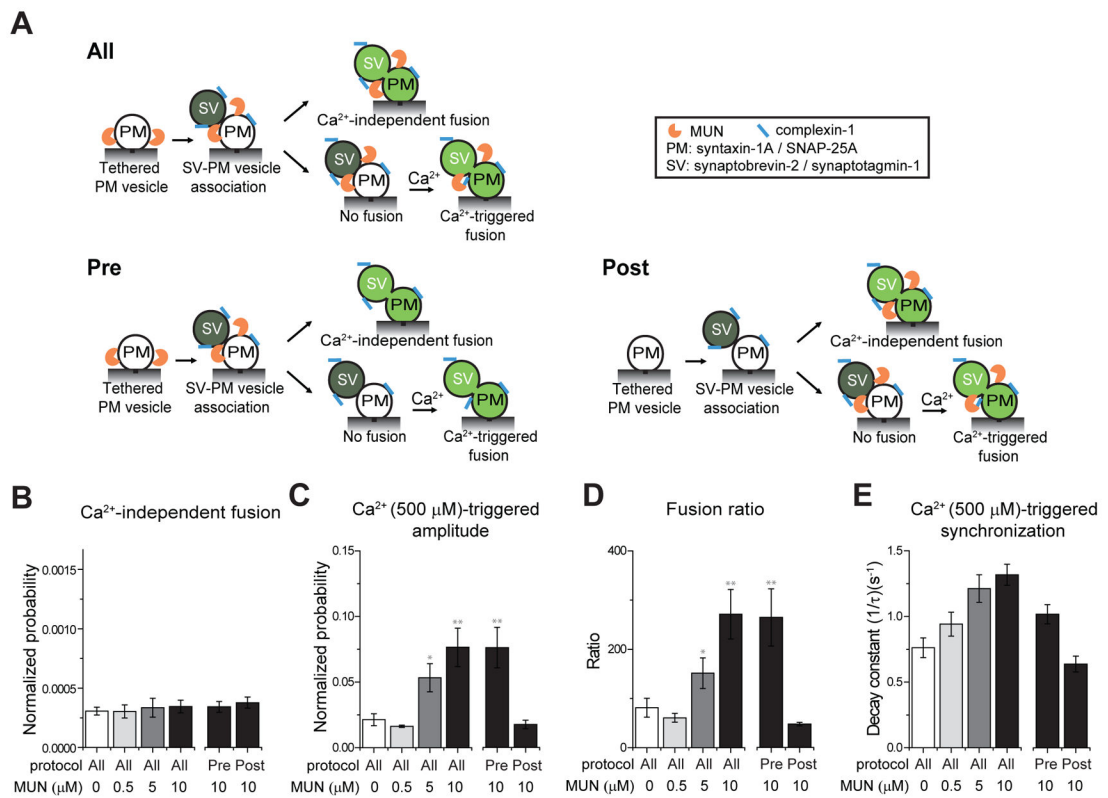


Figure 2. The MUN domain improves the efficiency of Ca²⁺-triggered fusion

(A) Single vesicle content mixing assay. PM: plasma membrane mimic vesicles with reconstituted syntaxin-1A and SNAP-25A; SV: synaptic vesicle mimic with reconstituted synaptobrevin-2 and synaptotagmin-1. After SV-PM vesicle association, vesicle pairs either undergo Ca²⁺-independent fusion or remain associated until fusion is triggered by Ca²⁺ addition. The MUN domain is only present during the specified stages. “0 μM MUN” refers to the absence of the MUN domain in all stages. In protocol “Pre” the MUN domain is only present before and during SV-PM vesicle association. In protocol “Post” the MUN domain is present only after SV-PM vesicle association. (B–E) The bar graphs show the effects of MUN domain on the average probability of Ca²⁺-independent fusion events per second (B), the amplitude of the first 1-sec time bin upon 500 μM Ca²⁺-injection (C), the ratio of the Ca²⁺-triggered amplitude to the average probably of Ca²⁺-independent fusion per second (D), and the decay rate (1/τ) of the Ca²⁺-triggered fusion histogram (E). The fusion probabilities and amplitudes were normalized to the number of analyzed SV-PM vesicle pairs (Table S3). Individual histograms are in Figure S2. Panels B–D show means ± SD for multiple independent repeat experiments (Table S33). (E) Decay constants and error estimates computed from the covariance matrix upon fitting the corresponding histograms with a single exponential decay function using the Levenberg-Marquardt algorithm. * p < 0.05, ** p < 0.01 by Student’s t-test, compared to the experiment without the MUN domain.

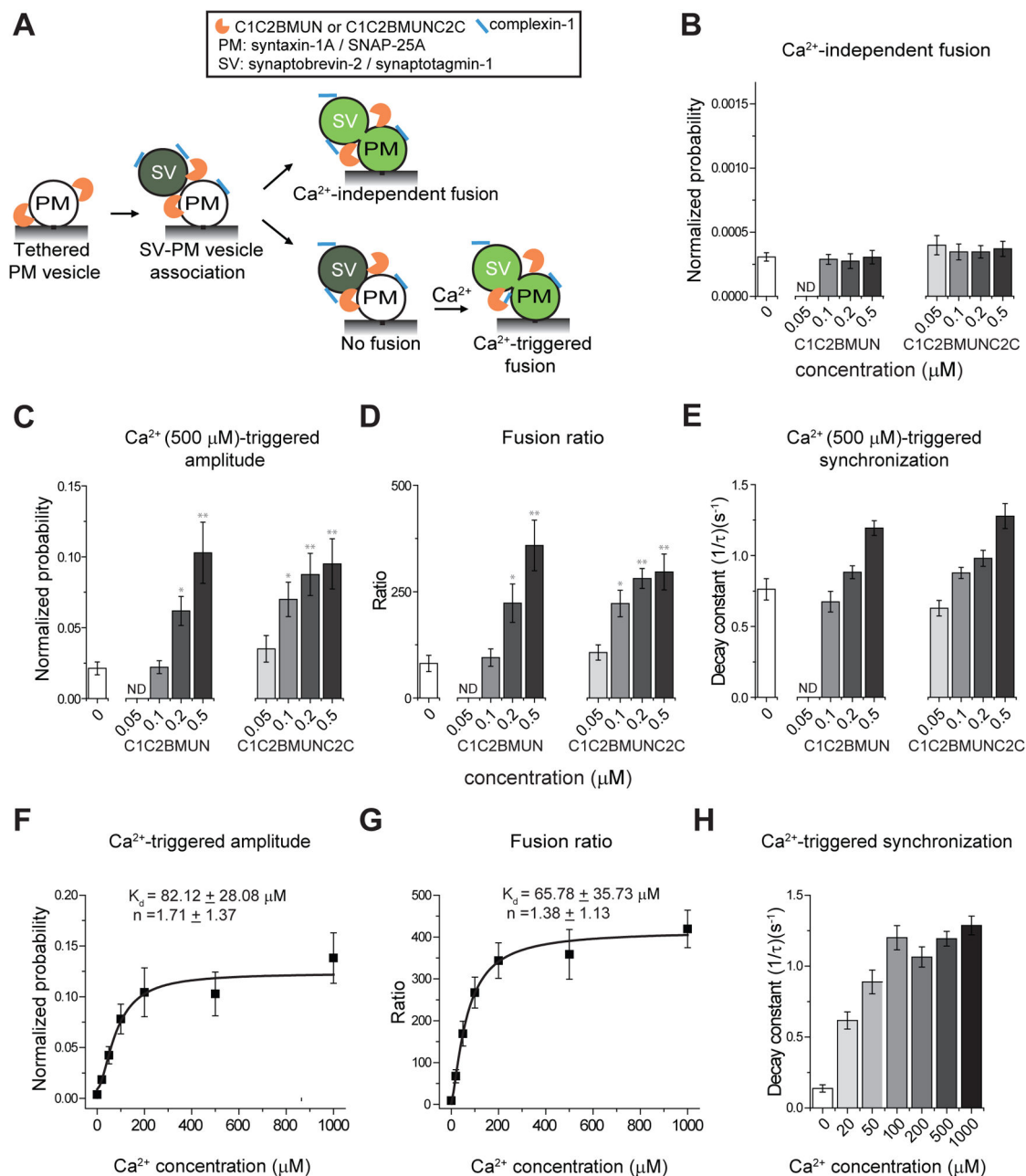


Figure 3. The C1C2BMUN and C1C2BMUNC2C fragments improve the efficiency of Ca²⁺-triggered fusion

(A) The experimental scheme is identical to that shown in Figure 2A, protocol “all”, except that the C1C2BMUN or the C1C2BMUNC2C fragment is used instead of the MUN domain. (B–E) The bar graphs show the effects of the C1C2BMUN or the C1C2BMUNC2C fragment on the average probability of Ca²⁺-independent fusion events per second (B), the amplitude of the first 1-sec time bin upon Ca²⁺-injection (C), the ratio of the Ca²⁺-triggered amplitude to the average probability of Ca²⁺-independent fusion per second (D), and the decay rate (1/τ) of the histogram upon Ca²⁺-injection (E). (F–H) Ca²⁺ concentration dependence of triggered fusion in the presence of 500 nM C1C2BMUN fragment. Shown are the

amplitude of the first 1-sec time bin upon 500 μM Ca^{2+} -injection (F), the ratio of the Ca^{2+} -triggered amplitude and the average probably of Ca^{2+} -independent fusion per second (G). F and G were fit to Hill functions yielding the Ca^{2+} concentration at half occupation K_d and the Hill coefficient n . (H) decay rate ($1/\tau$) of fusion histograms as a function of Ca^{2+} . The fusion probabilities and amplitudes were normalized to the number of analyzed SV-PM vesicle pairs (Table S4). Individual histograms are in Figure S2. Panels B–D and F–G show means \pm SD (Table S4). Panels E and H show decay constants and error estimates computed from the covariance matrix upon fitting the corresponding histograms with a single exponential decay function using the Levenberg-Marquardt algorithm. * $p < 0.05$, ** $p < 0.01$ by Student's t-test, compared to the experiment without the C1C2BMUN fragment.

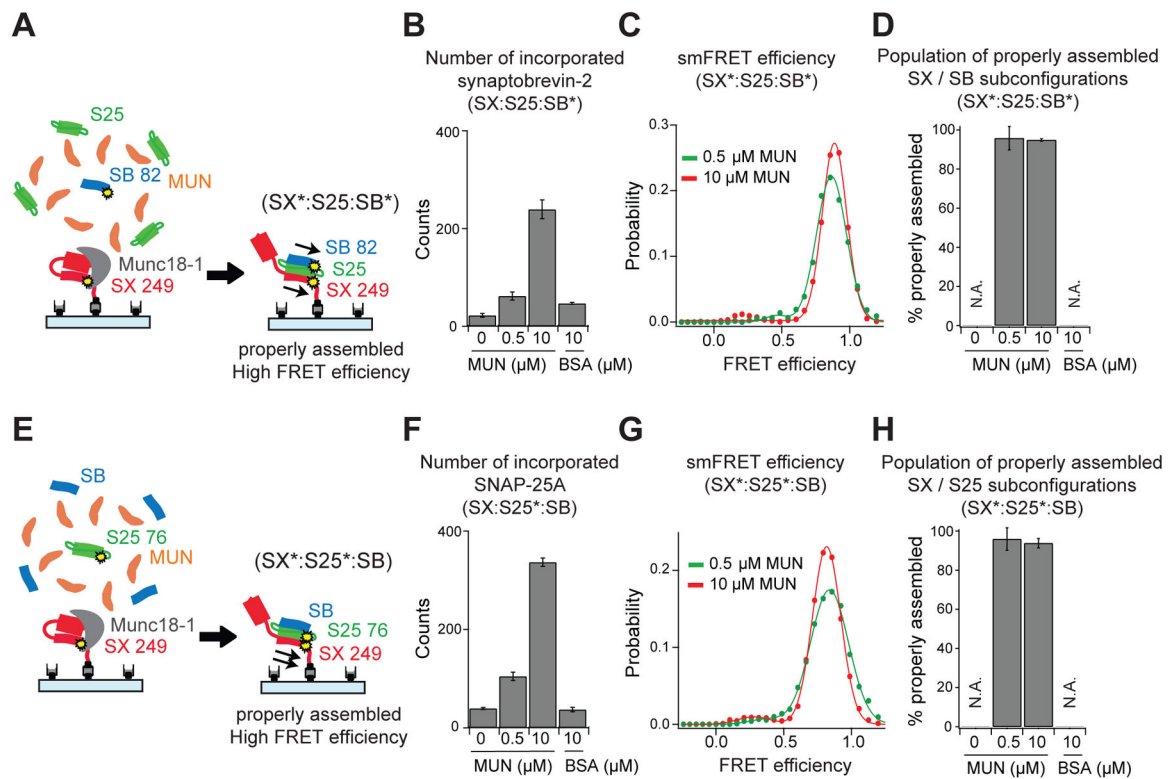
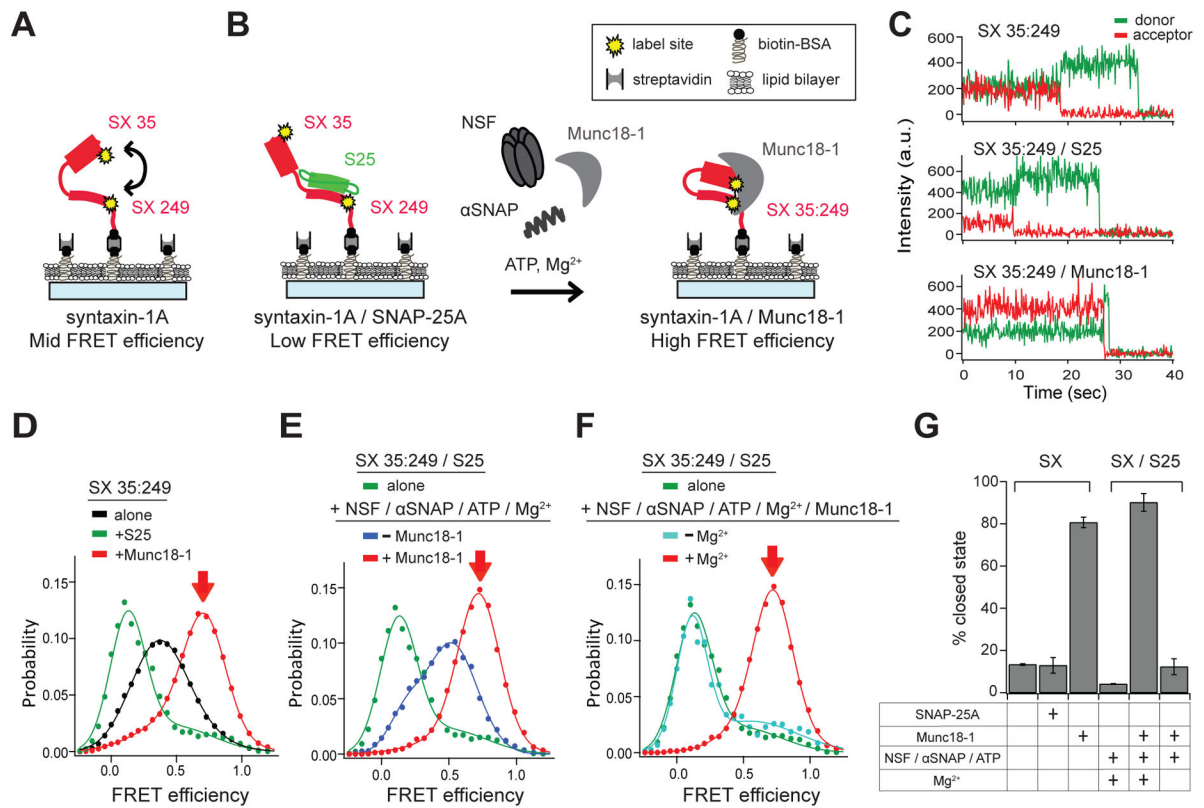


Figure 4. Munc13-1 and Munc18-1 promote proper assembly of the ternary SNARE complex
 (A) The configurations of the ternary SNARE complex were probed by single molecule experiments. The cytoplasmic domain of syntaxin-1A (SX) was tethered on a PEG-passivated microscope slide via streptavidin-biotin linkage. Munc18-1 was added to assemble the SX / Munc18-1 complex. SNAP-25A (S25), the cytoplasmic domain of synaptobrevin-2 (SB) were then added in the presence of the MUN domain at the specified concentration or BSA control. The yellow dots and the asterisks (*) indicate the fluorescently labeled residues. The thin arrows represent parallel SX / SB (A) or SX / S25 (E) subconfigurations. The labeling sites are SX residue 249, SB residue 82, and S25 residue 76. (B) Beginning with surface tethered SX / Munc18-1 complex, SB incorporation into the ternary SNARE complex was measured by counting the number of labeled (Alexa 555) SB molecules in presence of unlabeled S25 and the MUN domain at the specified concentrations or BSA control. (C) smFRET efficiency histograms for labels attached to SB (Alexa 555) and SX (Alexa 647) in the presence MUN at the specified concentrations. (D) Percent of properly assembled ternary SNARE subconfigurations. (E–H) Similar to panels (A–D), starting from surface tethered SX / Munc18-1 complex and forming ternary SNARE complex in the presence of unlabeled SB, labeled (Alexa 555) S25, and the MUN domain at the specified concentration or BSA control. Panels B, F show means of the counts from three fields of view \pm SD; panels D, H show means \pm SD for the two subsets of an equal partition of the data (Tables S1 and S2).



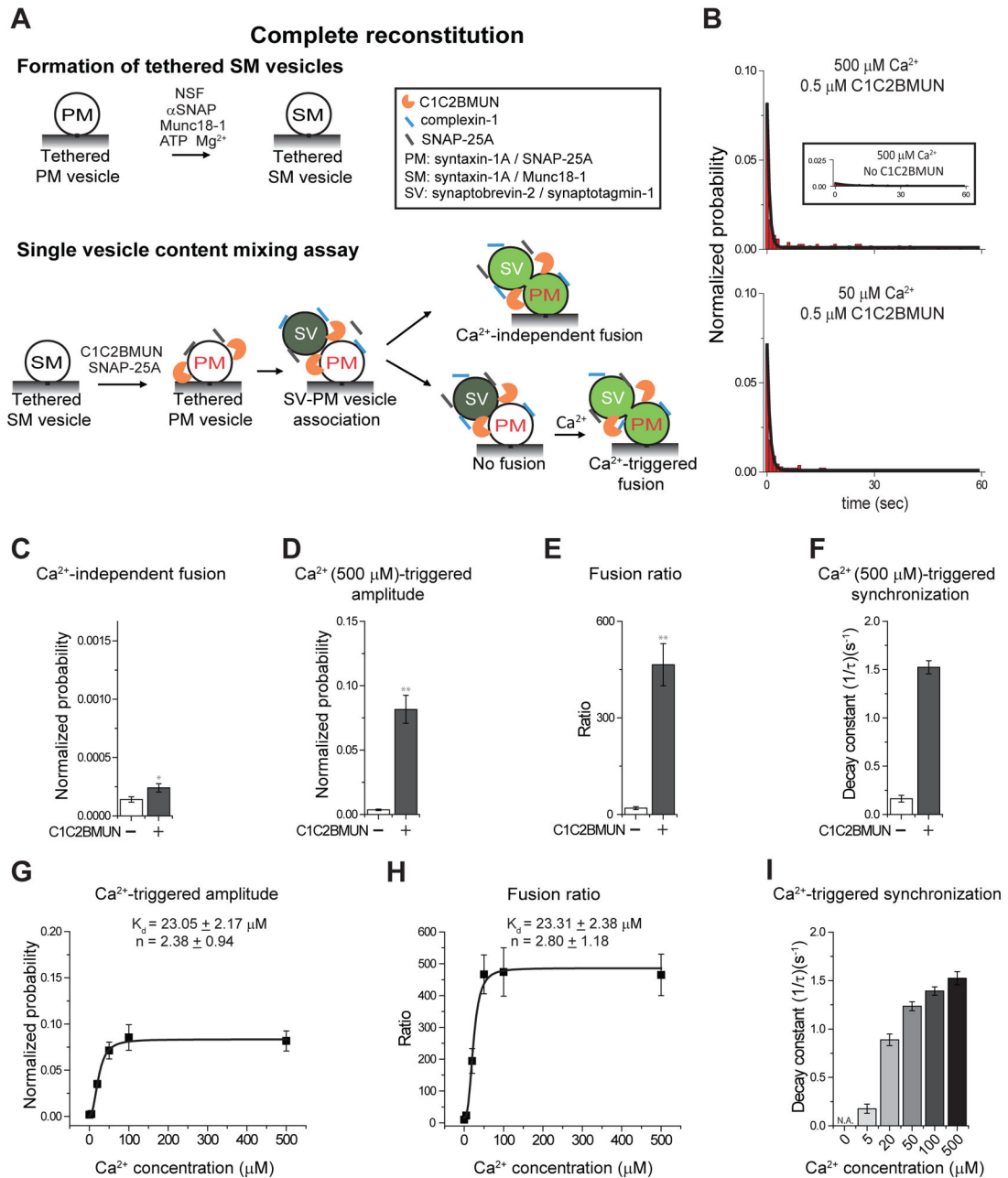


Figure 6. Fusion experiments with complete reconstitution

(A) Single vesicle content mixing assay with complete reconstitution. PM and SV defined in Figure 2; SM: vesicles with reconstituted syntaxin-1A / Munc18-1 complex. The C1C2BMUN fragment was added after formation of the SM vesicles and during all subsequent stages. (B) Representative histograms for triggered fusion at 50 μ M, 500 μ M Ca²⁺. Inset, triggered fusion without C1C2BMUN (note that without C1C2BMUN, ternary SNARE complex cannot form, thus little fusion is observed). (C–F) The bar graphs show the effects of C1C2BMUN fragment on the average probability of Ca²⁺-independent fusion events per second (C), the amplitude of the first 1-sec time bin upon 500 μ M Ca²⁺-injection

(D), the ratio of the Ca^{2+} -triggered amplitude to the average probably of Ca^{2+} -independent fusion per second (E), and the decay rate ($1/\tau$) of the histogram upon Ca^{2+} -injection (F). (G–I) Ca^{2+} concentration dependence of triggered fusion in the presence of 500 nM C1C2BMUN fragment. Shown are the amplitude of the first 1-sec time bin upon Ca^{2+} -injection (G), the ratio of the Ca^{2+} -triggered amplitude to the average probably of Ca^{2+} -independent fusion per second (H), and the decay rate ($1/\tau$) of the histogram upon Ca^{2+} -injection (I) as a function of Ca^{2+} -concentration. Hill functions were fit yielding the Ca^{2+} concentration at half occupation K_d and the Hill coefficient n . Individual histograms are in Figure S2. Panels C–E and G–H show means \pm SD for multiple independent repeat experiments (Table S7). Panels F and I show decay constants and error estimates computed from the covariance matrix upon fitting the corresponding histograms with a single exponential decay function using the Levenberg-Marquardt algorithm. * $p < 0.05$, ** $p < 0.01$ by Student's t-test.

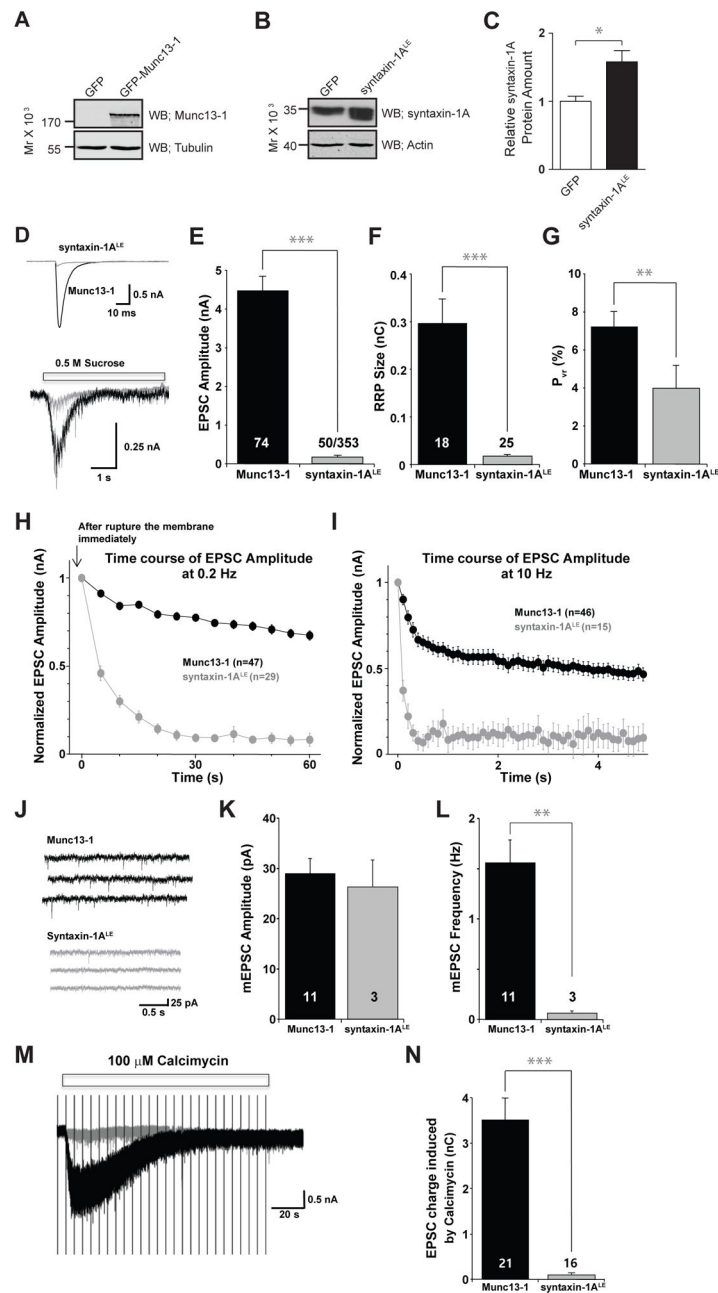


Figure 7. Syntaxin-1A^{LE} mutant overexpression in Munc13-1/2 double-knockout neurons
 Experiments in hippocampal autaptic neurons cultured from Munc13-1/2 double-knockout mice. Neurons were infected with recombinant Semliki Forest virus expressing either wild-type Munc13-1 or syntaxin-1A^{LE} mutant. (A) Western blot using an anti-Munc13-1 antibody showed the level of expression of Munc13-1 in Munc13-1/2 double-knockout hippocampal neurons infected with Semliki Forest virus expressing GFP only, or Munc13-1 (upper panel). Tubulin was used as a loading control (bottom panel). (B) Western blot using an anti-syntaxin-1A antibody showed the level of expression of syntaxin-1A/syntaxin-1A^{LE} in Munc13-1/2 double-knockout hippocampal neurons expressing GFP only syntaxin-1A^{LE}

(upper panel). Actin was used as a loading control (C) Relative quantification of syntaxin-1A protein amounts in Munc13-1/2 double-knockout hippocampal neurons. Signals were normalized to the level of endogenous syntaxin-1A in GFP-only overexpressing neurons (white bar; 1.0 ± 0.1 , $n=4$). Overexpression of syntaxin-1A^{LE} increase the signal 1.7 ± 0.2 fold (black bar; $n=3$, $p=0.037$ (Student's t-test)). (D) EPSCs were recorded in whole-cell patch-clamp mode. Representative traces of EPSCs (top) and postsynaptic currents evoked by 0.5 M sucrose (bottom). (E) Average values of EPSC amplitudes of the first three stimuli of a 0.2 Hz series of stimuli in neurons expressing Munc13-1 (black; from 74 neurons from 5 mice) and syntaxin-1A^{LE} mutant (grey; from 50 neurons from 5 mice) that showed a response out of 353 that expressed GFP). (F) Apparent readily releasable vesicle pool (RRP) size calculated by the integral of the sucrose response over 4 seconds in Munc13-1 (black; from 18 neurons from 3 mice) and syntaxin-1A^{LE} mutant neurons (grey; from 25 neurons from 3 mice). (G) Release probability calculated as the ratio of the EPSC amplitude to that of the RRP in Munc13-1 (black; from 18 neurons from 3 mice) and syntaxin-1A^{LE} mutant neurons (grey; from 25 neurons from 3 mice). (H) Normalized EPSC amplitudes in Munc13-1 wild type (black) and syntaxin-1A^{LE} mutant neurons (grey) during 0.2 Hz stimulation. (I) Normalized EPSC amplitudes during 10 Hz stimulation. (J) Representative traces of miniature EPSCs (mEPSC) in neurons with overexpressed Munc13-1 (top) or syntaxin-1A^{LE} mutant (bottom) in the presence of 200 nM TTX. (K) Average mEPSC amplitudes of Munc13-1 (black; from 11 neurons from 1 mouse) and syntaxin-1A^{LE} mutant neurons (grey; from 3 neurons from 1 mouse). (L) Average mEPSC frequencies of Munc13-1 (black) and syntaxin-1A^{LE} mutant neurons (grey). (M) Example traces of neurons in the presence of 100 μ M calcimycin. The vertical lines are stimulation artifacts resulting from intermittent monitoring of evoked EPSCs. (N) EPSC charge induced by calcimycin in Munc13-1 (from 21 neurons from 3 mice) and syntaxin-1A^{LE} mutant neurons (from 16 neurons from 4 mice). Note * $p<0.05$, ** $p<0.01$, and *** $p < 0.001$.

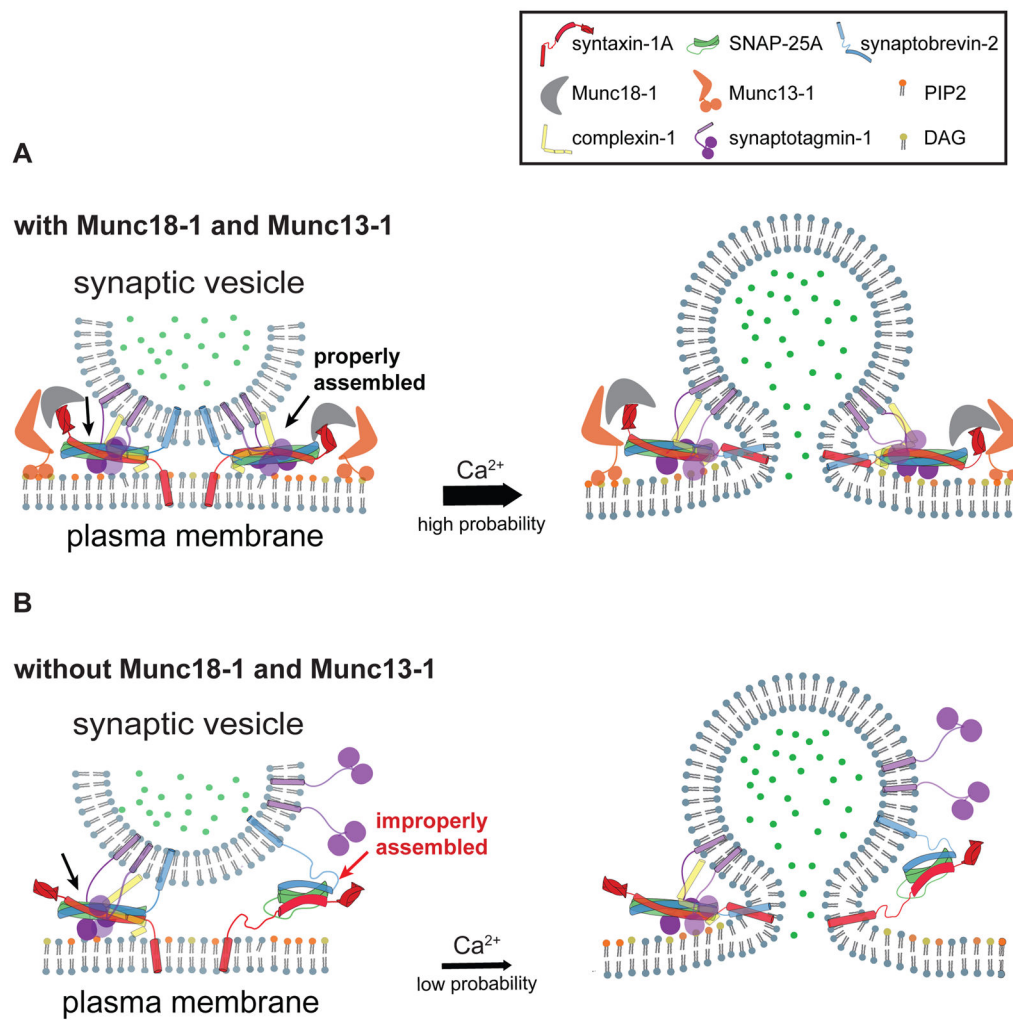


Figure 8. Model of concerted Munc18-1 / Munc13-1 action to properly assemble ternary SNARE complex

Model of the combined effect of Munc13-1 and Munc18-1 on Ca^{2+} -triggered fusion. (A) Munc13-1 and Munc18-1 cooperate to produce proper *trans* ternary SNARE complex. (B) Without Munc13-1 and Munc18-1, *trans* ternary SNARE complex assembly is error prone resulting in much reduced Ca^{2+} -triggered fusion probability.